MODIS Ocean Science Team

Algorithm Theoretical Basis Document

Case 2 Chlorophyll *a*

(ATBD-MOD-19)

Version 4

15 August 1997

Kendall L. Carder, Steve K. Hawes, Zhongping Lee and F. Robert Chen

Marine Science Department
University of South Florida
140 Seventh Avenue South
St. Petersburg, Florida 33701
kcarder@monty.marine.usf.edu

TABLE OF CONTENTS

1.0 Introduction

This document describes the Case 2 chlorophyll *a* algorithm. The algorithm is based on a semi-analytical, bio-optical model of remote-sensing reflectance, $R_{rs}(\lambda)$, where $R_{rs}(\lambda)$ is defined as the water-leaving radiance, $L_w(\lambda)$, divided by the downwelling irradiance just above the sea surface, $E_d(\lambda,0^+)$. The $R_{rs}(\lambda)$ model has two free parameters, the absorption coefficient due to phytoplankton at 675 nm, $a_\phi(675)$, and the absorption coefficient due to gelbstoff at 400 nm, $a_g(400)$. The R_{rs} model has many other parameters which are fixed, or can be specified based on the region and season of the MODIS scene. R_{rs} is modeled using these parameters at each of the visible-range MODIS wavelengths, λ_i. $R_{rs}(\lambda_i)$ is derived at each pixel from the normalized water-leaving radiance, $L_{wn}(\lambda_i)$, measured by MODIS. These $R_{rs}(\lambda_i)$ values are put into the model, the model is inverted, and $a_\phi(675)$ and $a_g(400)$ are computed. Chlorophyll *a* concentration is then derived simply from the $a_\phi(675)$ value. In highly turbid waters, an empirical algorithm is used to estimate chlorophyll concentration. The algorithm also outputs both the total absorption coefficients, $a(\lambda_i)$, and the phytoplankton absorption coefficients, $a_\phi(\lambda_i)$, at the visible MODIS wavelengths.

2.0 Overview and Background Information

According to the optical classification by Morel and Prieur (1977), oceanic waters may be characterized as Case 1, in which the optical properties are dominated by chlorophyll and associated and covarying detrital pigments, or as Case 2, in which other substances which do not covary with chlorophyll also affect the optical properties. Such substances include gelbstoff, suspended sediments, coccolithophores, detritus, and bacteria. Pigment retrievals from CZCS data in Case 1 waters have achieved reasonable results (± 40% for best cases, Gordon et al., 1983). However, the non-chlorophyll-covarying substances in Case 2 waters have caused the retrieval of pigment concentrations to have inaccuracies as high as 133% (Carder et al., 1991).

Marine colored dissolved organic matter (CDOM), also called gelbstoff, absorbs light in an exponentially decreasing manner as a function of wavelength. Pheopigments, detritus, and bacteria similarly absorb more strongly at 412 nm than they do at 443 nm. Phytoplankton, on the other hand, absorb more strongly at 443 nm than at 412 nm. Absorption largely determines the amount of light that exits the sea surface at each wavelength. Thus, by measuring the relative amounts of light leaving the sea surface at those two wavelengths, we can estimate the relative amounts of phytoplankton and the detrital products mentioned above.

The R_{rs} model has a few parameters that cannot be fixed and applied to the entire globe, i.e., they

are site- and season-specific. This is due to the inherent variability of many bio-optical constituents. For example, absorption per unit chlorophyll by phytoplankton can change with species, and with nutrient and lighting conditions by as much as a factor of five (Morel and Bricaud, 1981; Carder et al., 1991; Morel et al., 1993). These same conditions can also effect the spectral shape of the absorption. Also, particle size and concentration both have a significant effect on the spectral backscattering coefficient, $b_b(\lambda)$, of ocean water. This is so because pure water backscatters as $\sim \lambda^{-4}$, large particles backscatter as $\sim \lambda^{-0}$, and smaller diameter detritus and bacteria backscatter with a spectral dependence somewhere in between the two (Morel and Ahn, 1990; 1991). Many of these factors covary, which allowed the simple wavelength-ratio algorithms of the CZCS (Gordon and Morel, 1983) to work fairly well. We have tried to understand many of these individual covariances and have developed empirical expressions for several individual bio-optical parameters. By analyzing individual components of the model, we can gain a deeper understanding of the processes.

Extensive field data sets are needed to allow seamless modification of the model parameters with time and space. The changes required will be due mostly to changes in the dominant plankton groups present and the subsequent effects on bio-optical parameters such as pigment packaging. Acquiring such data sets on a global scale should be a major community goal during the next few years. We have developed a scenario that can both guide the parameterization process and provide an initial implementation of the algorithm for much of the ocean (tropics, subtropics, and summer temperate). Parameterization for high-latitude and upwelling waters has also been developed, and a preliminary method to smoothly transition between regions will be implemented in Versions 2.0 and 2.1 of the algorithm code.

2.1 Experimental Objective

The main data product is chlorophyll *a* concentration, [chl *a*], which can be used as an indicator of plankton biomass, as an input to primary production models, or to trace oceanographic currents, jets, and plumes. Other output products are $a_\phi(675)$, $a_g(400)$, $a_\phi(\lambda_i)$, and $a(\lambda_i)$. $a_\phi(\lambda_i)$ is used in the IPAR/ARP MODIS algorithm. $a_g(400)$ by itself can be used to map river plumes, to determine diffuse attenuation at that wavelength, or to calculate dissolved organic carbon (DOC) standing stocks and fluxes. In order to calculate DOC, we need to know how DOC concentration is related to DOC absorption. As coastal, estuarine, and other Case 2 environments become increasingly recognized as important areas of study, algorithms that can deal with the complex bio-optical properties of these regions are required.

2.2 Historical Perspective

CZCS algorithms for estimating [chl *a*] plus pheophytin *a* concentrations perform quite well for regions of the ocean where scattering and absorbing components of seawater covary with these pigments, i.e., in Case 1 waters (Gordon and Morel, 1983; Gordon et al., 1983). A number of empirical and semi-analytical optical models have been developed to simulate the behavior of the underwater light field for such waters (Morel and Prieur, 1977; Baker and Smith, 1981; Baker and Smith, 1982; Gordon et al., 1988; Morel, 1988; Mitchell and Holm-Hansen, 1991). Such models have been used as the basis for classifying water types and/or for developing remote sensing algorithms.

However, the accuracies of these models decrease when environmental conditions depart from those representative of the data set used to empirically derive the covariance relationships. For instance, CDOM is produced when grazing, photolysis, and other mechanisms degrade the viable plant matter at and downstream from phytoplankton blooms. The CDOM-to-chlorophyll ratio will change dramatically for a parcel of upwelled water over a relatively short time, from chlorophyll-rich and CDOM-poor to CDOM-rich and chlorophyll-poor. Solid evidence for the occurrence of this scenario can be found in two separate studies. Peacock et al. (1988) found that absorption attributed to CDOM at 440 nm was at least 16 fold that due to phytoplankton pigments within an offshore jet from an upwelling region, whereas pigments were the dominant absorption agents at the upwelling center near the coast. Similarly, Carder et al. (1989) found that particulate absorption at 440 nm decreased 13 fold while CDOM absorption at 440 nm increased by 60% in ten days for a phytoplankton bloom tracked from the Mississippi River plume to Cape San Blas. This widely varying CDOM-to-chlorophyll ratio has a profound effect on upwelled radiance in the blue 443 nm band of the CZCS, and a smaller but still significant effect in the green 520 nm band. The correspondence in absorption at 443 nm and 520 nm between CDOM and chlorophyll creates erroneously high estimates of pigment concentration in those models which rely solely upon either of these spectral bands to indicate absorption due to phytoplankton.

Carder et al. (1991) proposed that a short wavelength channel at around 410 nm could be used to distinguish CDOM (and other degradation products) from chlorophyll. A channel at 412 nm will be available not only on MODIS, but also on the Ocean Color and Temperature Scanner (OCTS) and on the Sea-Viewing-Wide-Field-Sensor (SeaWiFS). The Case 2 chlorophyll *a* algorithm will be thoroughly tested during the SeaWiFS project.

2.3 Instrument Characteristics

The algorithm requires as input L_{wn} at the MODIS wavebands 8−13, centered at 412, 443, 488,

531, 551, and 667 nm, respectively. R_{rs} is easily derived from L_{wn} as $R_{rs} = L_{wn} F_0$, where F_0 is the extraterrestrial solar irradiance. The 1000 m resolution and near daily coverage of MODIS will allow the observation of meso-scale oceanographic features in coastal and estuarine environments, areas seen to be increasingly important in many marine science studies.

3.0 Algorithm Description

Morel and Gordon (1980) describe three approaches to interpret ocean color data in terms of the *in situ* optical constituents: empirical, semi-empirical, and analytical. In the analytical approach, radiative transfer theory provides a relationship between upwelling irradiance or radiance and the *in situ* constituents. Then constituent concentrations are derived from irradiance or radiance values measured at several wavelengths by inversion of the resultant system of equations. The Case 2 algorithm uses this approach and the term "semi-analytical" is invoked because pieces of the radiative model are expressed by empirical relationships.

3.1 Theoretical Description

3.1.1 Physics of Problem

After light enters the ocean, some of it is eventually scattered back up through the surface. This light is called the water-leaving radiance, $L_w(\lambda)$, and it can be detected from space. The magnitude, spectral variation, and angular distribution of this radiance depend on: the absorption and backscattering coefficients of the seawater, $a(\lambda)$ and $b_b(\lambda)$, respectively (known as the inherent optical properties); the downwelling irradiance incident on the sea surface, $E_d(\lambda,0^+)$; and the angular distribution of the light within the ocean. To make things easier, we divide seawater into three components, each one having distinct optical properties of its own. These components are the seawater itself (water and salts), the particle fraction, and the dissolved fraction. Fortunately, $a(\lambda)$ is simply equal to the sum of the absorption coefficients for each component, and, to first order, $b_b(\lambda)$ is equal to the sum of the backscattering coefficients. If we can accurately describe or model each spectrally distinct component of the absorption and backscattering coefficients, then we can determine the magnitude of each one from measurements of $L_w(\lambda)$ and $E_d(0^+,\lambda)$, given some assumptions about the angular distribution of light in the water. The key here is to accurately model the spectral behavior of $a(\lambda)$ for each component. The spectral behavior of $b_b(\lambda)$ is not as important.

3.1.2 Mathematical Description of Algorithm

3.1.2.1 R_{rs} Model

The R_{rs} model is given by the following general equation, which is adapted from Lee et al. (1994):

$$R_{rs}(\lambda) = \frac{f\ t^2}{Q(\lambda)\ n^2} \frac{b_b(\lambda)}{[a(\lambda) + b_b(\lambda)]} \quad (1)$$

where f is an empirical factor averaging about 0.32–0.33 (Gordon et al., 1975; Morel and Prieur, 1977; Jerome et al., 1988; Kirk, 1991), t is the transmittance of the air-sea interface, Q(λ) is the upwelling irradiance-to-radiance ratio $E_u(\lambda)/L_u(\lambda)$, and n is the real part of the index of refraction of seawater. By making three approximations, Eq. 1 can be greatly simplified.

1) In general, f is a function of the solar zenith angle, θ_0 (Kirk, 1984; Jerome et al., 1988; Morel and Gentili, 1991). However, Morel and Gentili (1993) have shown that the ratio f/Q is relatively independent of θ_0 for sun and satellite viewing angles expected for the MODIS orbit. They estimate that f/Q = 0.0936, 0.0944, 0.0929, and 0.0881, (standard deviation ± 0.005), for λ = 440, 500, 565, and 665 nm, respectively. Also, Gordon et al. (1988) estimates that f/Q = 0.0949, at least for $\theta_0 \geq 20°$. Thus, we assume that f/Q is independent of λ and θ_0 for all MODIS wavebands of interest, except perhaps for the band centered at 667 nm.

2) t^2/n^2 is approximately equal to 0.54, and although it can change with sea-state (Austin, 1974), it is relatively independent of wavelength.

3) Many studies have confirmed that $b_b(\lambda)$ is usually much smaller than $a(\lambda)$ and can thus be safely removed from the denominator of Eq. 1 (Morel and Prieur, 1977; references cited in Gordon and Morel, 1983), except for highly turbid waters.

These three approximations lead to a simplified version of Eq. 1,

$$R_{rs}(\lambda) \approx constant\ \frac{b_b(\lambda)}{a(\lambda)} \quad (2)$$

where the "constant" is unchanging with respect to λ and θ_0. The value of the constant is not relevant to the algorithm since, as will be shown later, the algorithm uses spectral ratios of $R_{rs}(\lambda)$ and the constant term factors out.

In the following sections, both $b_b(\lambda)$ and $a(\lambda)$ will be divided into several separate terms. Each

term will be described empirically. The equations are written in a general fashion — i.e., the empirically derived parameters that describe each term are written as variables — and the actual values of the parameters that are used in the algorithm are shown in Table 1.

3.1.2.2 Backscattering Term

The total backscattering coefficient, $b_b(\lambda)$, can be expanded as

$$b_b(\lambda) = b_{bw}(\lambda) + b_{bp}(\lambda) \tag{3}$$

where the subscripts "w" and "p" refer to water and particles, respectively. $b_{bw}(\lambda)$ is constant and well known (Smith and Baker, 1981). $b_{bp}(\lambda)$ is modeled as

$$b_{bp}(\lambda) = X\left[\frac{551}{\lambda}\right]^{Y} \tag{4}$$

The magnitude of particle backscattering is indicated by X, which is approximately equal to $b_{bp}(555)$, while Y describes the spectral shape of the particle backscattering.

We now need to develop expressions for X and Y. To do this, we turn to the work of Lee et al. (1994). They use a slightly different form of the R_{rs} model, summarized by the following three equations:

$$R_{rs}(\lambda) = \frac{0.176\, b_b(\lambda)}{Q(\lambda)\, a(\lambda)} \tag{5}$$

$$\frac{b_b(\lambda)}{Q(\lambda)} \approx \frac{b_{bw}(\lambda)}{Q_w(\lambda)} + \frac{b_{bp}(\lambda)}{Q_p(\lambda)} \tag{6}$$

$$\frac{b_{bp}(\lambda)}{Q_p(\lambda)} = X'\left[\frac{400}{\lambda}\right]^{Y'} \tag{7}$$

The main differences here are that b_b/Q is modeled explicitly rather than just b_b (compare Eqs. 3 and 6), and that 400 nm is used rather than 551 nm as the normalizing point in the particle backscattering term

(compare Eqs. 4 and 7). Eq. 6 is an approximation derived from single and quasi-single scattering theory (Lee et al., 1994).

They developed a method to determine X' and Y' empirically for a given optical station by model inversion. The method uses measured values of $R_{rs}(\lambda)$ and $a(\lambda)$ at $\approx$ 200 wavelengths. The best-fit values for X' and Y' are determined using Eqs. 5–7 on a station-by-station basis. Using this method we determined X' and Y' for a number of optical stations taken from 4 separate cruises to the Gulf of Mexico. We then converted the X' and Y' values to our X and Y via

$$X = X' Q_p \left[\frac{400}{551}\right]^{Y'}$$
$$Y = Y' \qquad (8)$$

using a value of 3.55 for Q_p. Next, the converted X and Y values were compared to the $R_{rs}(\lambda)$ values measured at the corresponding station with the purpose of finding empirical relationships for both X and Y as a function of $R_{rs}(\lambda)$ at one or more of the MODIS wavelengths. Once this is done, X and Y can be estimated from MODIS data. These empirical relationships are described below.

3.1.2.2.1 Expression for X

Since X is approximately proportional to the magnitude of the particle backscattering, X should covary with R_{rs} at one of the longer MODIS wavelengths, i.e., at 551 or 667 nm. This is so because at these wavelengths water absorption dominates $a(\lambda)$ and R_{rs} becomes approximately proportional to b_b (see Eq. 2), at least for non-turbid waters. We chose the 551 nm channel because the 667 nm channel may be contaminated by chlorophyll fluorescence and because the water absorption at 667 nm is so high that the water-leaving radiance signal there may be too small to be accurate.

The general expression for X is

$$X = X_0 + X_1 R_{rs}(551) \qquad (9)$$

where X_0 and X_1 are empirically derived constants. Linear regression performed on the derived values of X vs. $R_{rs}(551)$ taken from four cruises to the Gulf of Mexico (CP92, Tambax 2, GOMEX, and COLOR)

resulted in X_0 and X_1 values of −0.00182 and 2.058 (n = 53, r^2 = 0.96). Figure 1 shows the regression graphically. If X is determined to be negative from Eq. 9 it is set to zero.

The values of X_0 and X_1 that are used in this version of the Case 2 chlorophyll algorithm are probably adequate for most of the globe and they are listed in Table 1. For regions influenced by rivers outflows, these parameters should be determined on a site-specific basis.

3.1.2.2.2 Expression for Y

Y was found to covary in a rather general way with the ratio $R_{rs}(443)/R_{rs}(488)$. Variations in numerator and denominator values of this ratio are largely determined by absorption due to phytoplankton and CDOM. Absorption due to water is about the same and low at both wavelengths. Thus, to the extent that phytoplankton and CDOM absorption covary, the spectral ratio of the absorption coefficients, a(443)/a(488), will be only weakly dependent on pigment concentration. Therefore, the spectral ratio of backscattering coefficients should have a significant effect on the spectral ratio of R_{rs} at these wavelengths. Y is thus represented as a linear function of $R_{rs}(443)/R_{rs}(488)$,

$$Y = Y_0 + Y_1 \frac{R_{rs}(443)}{R_{rs}(488)} \tag{10}$$

where Y_0 and Y_1 are empirically derived constants.

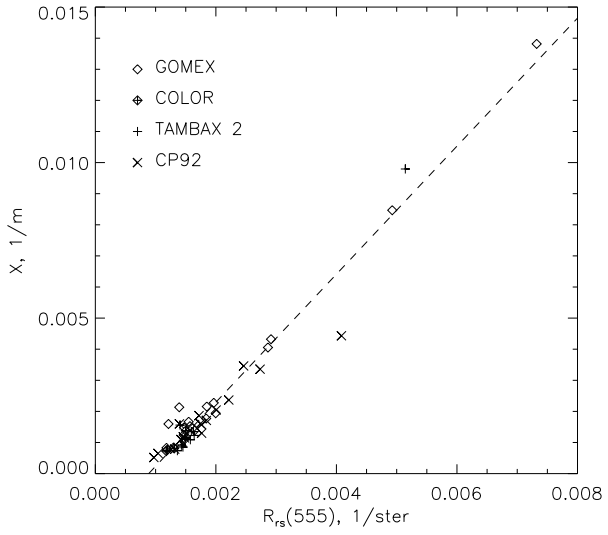

Figure 1. X vs. $R_{rs}(551)$. The line is the linear regression equation X = –0.00182 + 2.058 $R_{rs}(551)$ (n = 53, r^2 = 0.96).

Accurate measurements of $a_g(\lambda)$ and accurate removal of reflected skylight from the R_{rs} measurements are critical in determining Y by model inversion. Only data from the GOMEX and COLOR cruises are used here because the $a_g(\lambda)$ values were determined with a long-path spectrophotometer (Peacock et al., 1994). Linear regression of Y on $R_{rs}(443)/R_{rs}(488)$ for stations from these two cruises resulted in Y_0 and Y_1 values of −1.13 and 2.57 (n = 22, r^2 = 0.59). Figure 2 shows the regression graphically. If Y is determined to be negative from Eq. 10 it is set to zero. A number of other spectral ratios of $R_{rs}(\lambda)$ were tested, but the 443:488 ratio had the highest correlation with Y. The sensitivity of this method to errors in $a_g(\lambda)$ and reflected skylight estimates likely accounts for some of the scatter about the regression line.

The Y parameter should be large when the backscattering is due to small particles and/or water and vice versa (Gordon and Morel, 1983). In oligotrophic regions we have determined values of Y greater than 2, while in waters with [chl *a*] > 10 mg m^{-3} the estimated Y values are often ≈ 0.

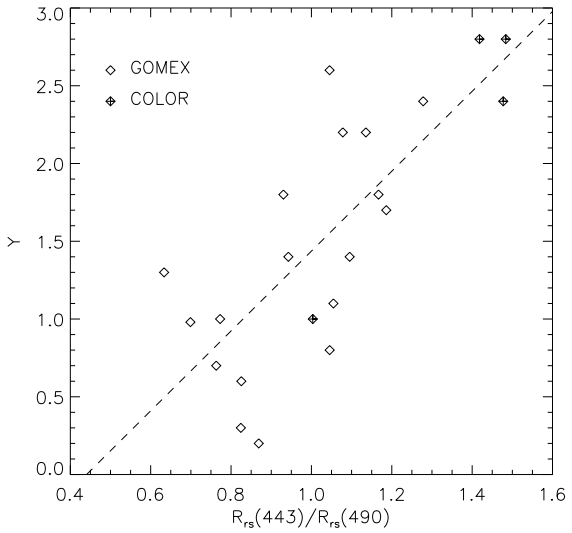

Figure 2. Y vs. $R_{rs}(443)/R_{rs}(488)$. The line is the linear regression Y = −1.13 + 2.57 $R_{rs}(443)/R_{rs}(488)$ (n = 22, r^2= 0.59).

3.1.2.3 Absorption Term

The total absorption coefficient can be expanded as

$$a(\lambda) = a_w(\lambda) + a_\varphi(\lambda) + a_d(\lambda) + a_g(\lambda) \qquad (11)$$

where the subscripts "w", "ϕ," "d," and "g" refer to water, phytoplankton, detritus, and CDOM ("g"

stands for gelbstoff). $a_w(\lambda)$ is taken from Pope et al. (1997). Expressions for $a_\phi(\lambda)$, $a_d(\lambda)$, and $a_g(\lambda)$ need to be developed.

3.1.2.3.1 Expression for a_ϕ

The shape of the $a_\phi(\lambda)$ spectrum for a given water-mass will change due to the pigment-package effect (i.e., the flattening of absorption peaks with increasing intracellular pigment concentration due to self-shading; Morel and Bricaud, 1981) and due to changes in pigment composition. We have found that for a given region and season, normalizing measured $a_\phi(\lambda)$ curves to $a_\phi(675)$ results in a smooth variation for $a_\phi(\lambda)/a_\phi(675)$ vs. $a_\phi(675)$ for the MODIS wavebands centered at λ = 412, 443, 488, 531, and 551 nm (see Figure 3). This relationship describes the packaging and pigment effects better than the relationship between $a_\phi^*(\lambda)$ and [chl *a*] that was used in previous versions of this algorithm. This is so because the $a_\phi^*(\lambda)$ vs. [chl *a*] relationship requires two separate measurements for each data point — $a_\phi(\lambda)$ and [chl *a*] — whereas the $a_\phi(\lambda)/a_\phi(675)$ vs. $a_\phi(675)$ relationship requires only the $a_\phi(\lambda)$ measurement.

A hyperbolic tangent function was chosen to model this relationship in order to ensure that the value of $a_\phi(\lambda)/a_\phi(675)$ approaches an asymptote at very high or very low values of $a_\phi(675)$ (Carder et al., 1991). Using logarithmic scaling for both axes results in the following model equation for $a_\phi(\lambda)$ as a function of $a_\phi(675)$,

$$a_\varphi(\lambda) = a_0(\lambda)\exp\left[a_1(\lambda)\tanh\left[a_2(\lambda)\ln\left(a_\varphi(675)/a_3(\lambda)\right)\right]\right]-a_\varphi(675) \qquad (12)$$

where the parameters $a_0(\lambda)$–$a_3(\lambda)$ are empirically determined for each MODIS wavelength of interest. $a_0(\lambda)$ is the most important of these parameters, as it is directly proportional to $a_\phi(\lambda)$. For simplicity, only $a_0(\lambda)$ and $a_1(\lambda)$ are varied to parameterize $a_\phi(\lambda)$, with $a_2(\lambda)$ and $a_3(\lambda)$ being set to the constant values of –0.5 and 0.010, respectively. Figure 3 shows the measured data and the modeled curves for $a_\phi(\lambda)$ measurements taken from the GOMEX, COLOR, and TN048 cruises. The parameters $a_0(\lambda)$–$a_3(\lambda)$ are listed in Table 1.

The method used to determine absorption coefficients for particles and for detritus involves filtering as much as 4 liters of water through a 25 mm diameter, Gelman glass-fiber filter (GFF). This large amount of water is used to concentrate the sample enough for accurate measurements of the pad

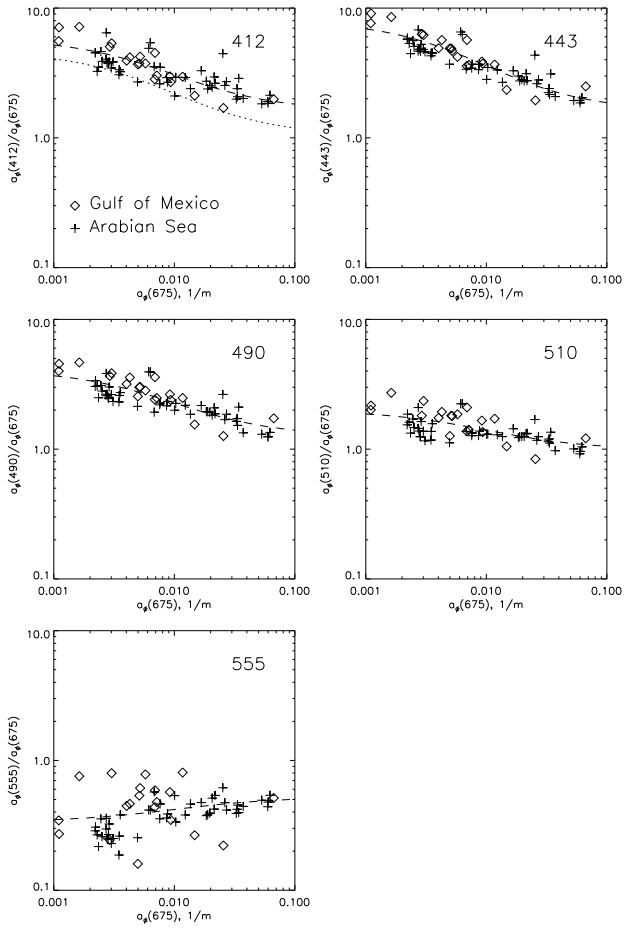

Figure 3. $a_\phi(\lambda)/a_\phi(675)$ vs. $a_\phi(675)$ for each MODIS waveband. The number in the top right corner indicates λ. The lines are described by Eq. 12 using the parameters listed in Table 1, and they represent the minimum sum of squared errors for modeled vs. measured values of $a_\phi(\lambda)/a_\phi(675)$.

optical density (OD) to be determined (Shibata, 1958; Mitchell, 1990; Nelson and Robertson, 1993; Moore et al., 1995). In order to estimate absorption coefficients from the OD measurements, an optical path elongation factor, called ≥, which is dependent upon OD, is employed. Recently however, it has been shown that ≥ varies with the particle size prevalent to a region (Moore et al., 1995). This happens because smaller particles get deeply imbedded into the pad, providing a greater absorption cross-section for photons scattered numerous times than for the large particles remaining at the surface of the pad. For our work, we chose a ≥ factor appropriate for small, subtropical particles by averaging two published ≥ factors, one developed for detritus (Nelson and Robertson, 1993) and one for synechococcus (Moore et al., 1995). Our ≥ factor is

$$\beta = 1.0 + 0.6\,OD^{-0.5} \quad (13)$$

3.1.2.3.2 Expression for a_d and a_g

$a_d(\lambda)$ and $a_g(\lambda)$ can both be fit to a curve of the form $a_x(\lambda) = a_x(400)\exp[-S_x(\lambda-400)]$ where the subscript "x" refers to either "d" or "g" (Bricaud et al., 1981; Roesler et al., 1989; Carder et al., 1991). Due to this similarity in spectral shape, the $a_d(\lambda)$ term can be eliminated, allowing both detrital and CDOM absorption to be represented by $a_g(\lambda)$. The combined CDOM and detritus absorption term is thus written

$$a_g(\lambda) = a_g(400)\,exp^{-S(\lambda-400)} \quad (14)$$

where S is empirically determined. Many researchers have reported that $S_d = 0.011$ nm^{-1}, on average (Roesler et al., 1989). For the GOMEX and COLOR cruises, an average value of 0.017 nm^{-1} was measured for S_g. Values reported by F. Hoge (personal communication) for the Sargasso Sea were somewhat higher as are those found near swampy regions of the Gulf of Mexico. The algorithm performance was optimized by varying S_g, with the value 0.019 nm^{-1} providing the smallest residual error compared to field measurements.

As a final note on the R_{rs} model, Eqs. 9–12, and 14 are written in a general way to emphasize that the values of the parameters X_0, X_1, Y_0, Y_1, a_0, a_1, and S are not meant to be absolute. They should be updated and changed as more data become available. These parameters may also be changed with region and season to optimize algorithm performance.

3.1.2.4 Inverting the Model

All of the pieces of the reflectance model are now in place. Via Eqs. 2–4, 9–12, and 14, $R_{rs}(\lambda)$ can be expressed solely as a function of the "constant" term, $R_{rs}(443)$, $R_{rs}(488)$, $R_{rs}(551)$, $a_\phi(675)$, and $a_g(400)$, given values for the parameters for X_0, X_1, Y_0, Y_1, $a_0(\lambda)$, $a_1(\lambda)$, and S. $L_{wn}(\lambda)$ from MODIS can be converted into $R_{rs}(\lambda)$ as mentioned previously. Then, for each pixel, the R_{rs} model equation can be written for each of the 5 available MODIS wavebands yielding 5 equations written in 3 unknowns: the "constant" term, $a_\phi(675)$, and $a_g(400)$.

Using spectral ratios of R_{rs} eliminates the "constant" term, since it is largely independent of

wavelength. In principle, two spectral ratio equations can be used to solve for the two remaining unknowns, $a_\phi(675)$ and $a_g(400)$. Based on the shape of the absorption curve for phytoplankton versus those for CDOM and detritus, equations using spectral ratios of 412:443 and 443:551 for $R_{rs}(\lambda)$ should provide a good separation of the two absorption contributions. Our two equations are

$$\frac{R_{rs}(412)}{R_{rs}(443)} = \frac{b_b(412)}{b_b(443)} \frac{a(443)}{a(412)}$$

$$\frac{R_{rs}(443)}{R_{rs}(551)} = \frac{b_b(443)}{b_b(551)} \frac{a(551)}{a(443)} \quad (15)$$

The right-hand side of each equation is a function of $a_\phi(675)$, $a_g(400)$, $R_{rs}(443)$, $R_{rs}(488)$ and $R_{rs}(551)$. Since the R_{rs} values are provided on input, we now have two equations in two unknowns. The equations can usually be solved algebraically to provide values for $a_\phi(675)$ and $a_g(400)$. The computational method of solving these equations is described in Section 3.2.1.

For waters with high concentrations of CDOM and chlorophyll, $L_w(412)$ and $L_w(443)$ values are small, and the semi-analytical algorithm cannot perform properly. It is thus designed to return values only when modeled $a_\phi(675)$ is less than 0.06 m^{-1}, which is equivalent to [chl *a*] of about 3–4 mg m^{-3}. Otherwise, an empirical algorithm for [chl *a*] is used, which is described in Section 3.1.2.6. There is presently no output for $a_\phi(675)$ and $a_g(400)$ when the empirical [chl *a*] algorithm is employed, but empirical algorithms for these variables are under development.

3.1.2.5 Pigment Algorithm for Semi-analytical Case

When the semi-analytical algorithm returns a value for $a_\phi(675)$, [chl *a*] is determined via a direct relationship to this value. This step requires precise knowledge of the chlorophyll-specific absorption coefficient for phytoplankton at 675 nm, $a_\phi^*(675)$. [chl *a*] vs. $a_\phi(675)$ data used to examine this relationship must be internally consistent. For example, due to self-shading or pigment-packaging (Morel and Bricaud, 1981), pigments *in vivo* (still within the cells) should never absorb more than the same pigments *in vitro* (extracted from the cells) once solvent effects are accounted for, yet the literature is replete with *in vivo* $a_\phi^*(675)$ measurements far exceeding 0.025 m^2 [mg chl *a*]$^{-1}$. This value is higher than the *in vitro* specific absorption coefficient at the red peak for pure chlorophyll *a* in solution, which is about 0.0203 m^2 [mg chl *a*]$^{-1}$ for solution in acetone (Jeffrey and Humphrey, 1975) and about 0.0171

m^2 [mg chl *a*]$^{-1}$ for solution in methanol (unpublished results from our lab), but it allows for some absorption by pheopigments and accessory pigments.

To evaluate variations of $a_\phi(675)$ with [chl *a*], we developed our own subtropical data set to explore some of the variation in $a_\phi^*(675)$ under high-light conditions. This data set came from surface water samples from several Gulf of Mexico cruises (BONG 1, BONG 2, BOSS 1, and WFS) and one cruise to the Arabian Sea (TN048). Linear regression of log([chl *a*]) vs. log($a_\phi(675)$) yields an equation of the form

$$[chl\ a] = P_0 * [\ a_\varphi(675)]^{p_1} \quad (16)$$

For the data set mentioned above, the regression resulted in p_0 and p_1 values of 56.8 and 1.03 (n = 95, r^2= 0.97 on the log-transformed values). This regression and the data are shown in Figure 4. These values were adjusted slightly to 51.9 and 1.00, respectively, to simplify by elimination of the nonlinear term for use with global, subtropical data sets.

3.1.2.6 Pigment Algorithm for the Default Case

When the semi-analytical algorithm does not return a value for $a_\phi(675)$, we provide an empirical, two-wavelength algorithm for [chl *a*] to use by default. Aiken et al. (1995) found that the $L_w(488)/L_w(551)$ ratio is best for empirical [chl *a*] determination. We use an equation of the form

$$log[chl\ a]_{emp} = c_0 + c_1\ log(r_{35}) + c_2\ [log(r_{35})]^2 + c_3\ [log(r_{35})]^3 \quad (17)$$

where

$$r_{35} = \frac{R_{rs}(488)}{R_{rs}(551)} \quad (18)$$

[chl *a*]$_{emp}$ is called the "empirically-derived" or "default" chlorophyll *a* concentration, and c_0, c_1, and c_2 are empirically derived constants.

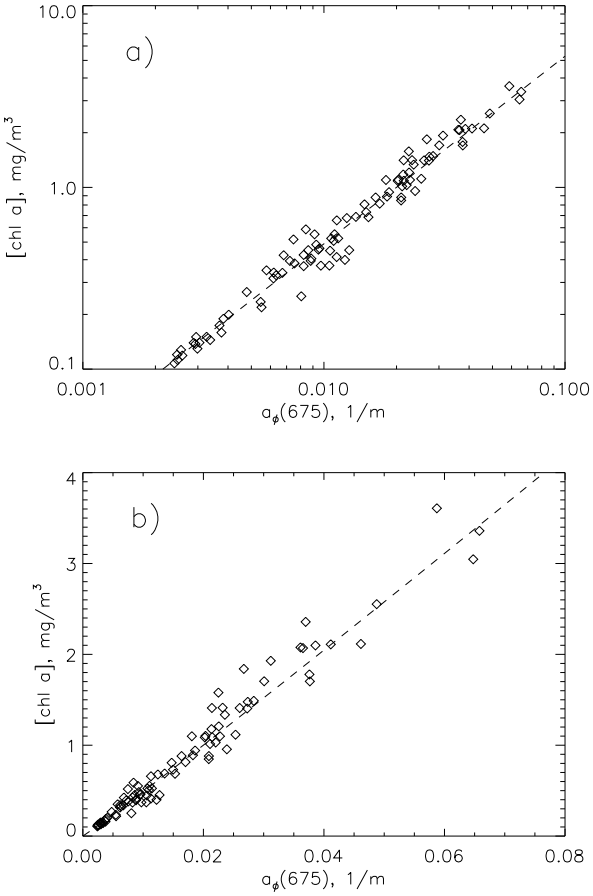

Figure 4. [chl *a*] vs. $a_\phi(675)$ a) in logarithmic scaling and b) in normal scaling. In both charts the line is the equation $[\text{chl } a] = 56.8[a_\phi(675)]^{1.03}$. This equation is the result of linear regression on the log-transformed values (n = 96, r^2 = 0.97).

A subtropical and temperate summer data set was constructed from stations from the MLML 2, GOMEX, COLOR, and TN042 cruises, and from stations below 45 °N from the TT010 cruise (Table 2). This data set includes both open-ocean and riverine-influenced stations. Quadratic regression of log([chl *a*]) against log(r_{35}) for measured [chl *a*] and $R_{rs}(\lambda)$ in this data set resulted in values of $c_0 = 0.289$, $c_1 = -3.20$, $c_2 = 1.20$, and $c_3 = 0.00$ (n = 62), yielding a root mean square (RMS) error of 0.51. The data and the regression line are shown in Figure 5.

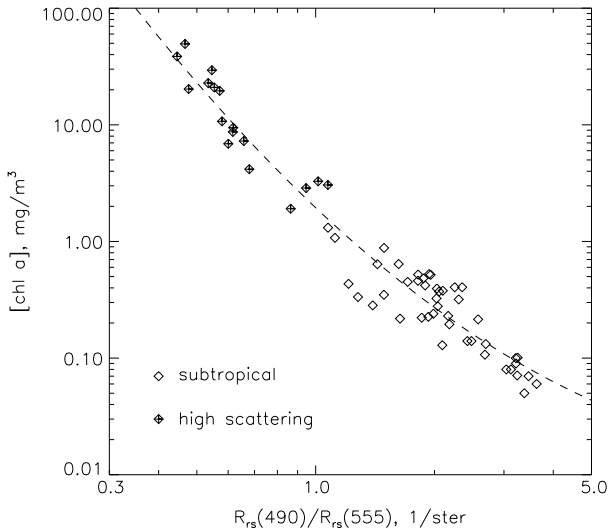

Figure 5. [chl *a*] vs. $R_{rs}(488)/R_{rs}(551)$ in log-log scaling. The line represents a quadratic regression on the log-transformed value. This line describes the default [chl *a*] algorithm.

3.1.2.7 Weighted Pigment Algorithm

Another consideration is that there should be a smooth transition in [chl *a*] values when the algorithm switches from the semi-analytical to the empirical method. This is achieved by using a weighted average of the [chl *a*] values returned by the two algorithms when near the transition border. When the semi-analytical algorithm returns an $a_\phi(675)$ value between 0.015 and 0.03 m^{-1}, [chl *a*] is calculated as

$$[chl\ a] = w\,[chl\ a]_{sa} + (1 - w)[chl\ a]_{emp} \tag{19}$$

where $[chl\ a]_{sa}$ is the semi-analytically-derived value and $[chl\ a]_{emp}$ is the empirically derived value, and the weighting factor is $w = [0.03 - a_\phi(675)]/0.015$.

3.1.2.8 Total and Phytoplankton Absorption Coefficients

The phytoplankton absorption coefficients, $a_\phi(\lambda_i)$, are calculated by inserting the modeled $a_\phi(675)$ value into Eq. 12 and using the necessary parameters from Table 1 for each wavelength. The

total absorption coefficients, $a(\lambda_i)$, are calculated by inserting the modeled $a_g(400)$ value and the S parameter from Table 1 into Eq. 14 to get $a_g(\lambda_i)$, then combining them with the $a_\phi(\lambda_i)$ values in Eq. 11.

3.2 Numerical computation

$a_\phi(675)$ and $a_g(400)$ are determined from Eq. 15 by inverting one of the equations to isolate $a_g(400)$, substituting into the other equation, and moving all terms to one side, yielding a function that depends only on $a_\phi(675)$ (given values for R_{rs} and Table 1 for the algorithm parameters). The value of $a_\phi(675)$ at which the function crosses zero is the solution we seek. This solution is determined computationally via the bisection method. A 33-element array of $a_\phi(675)$ values, scaled logarithmically from 0.0001 to 0.06 m^{-1} is created, and the function is evaluated at the two extrema. If the function changes sign between the two outermost values, a solution exists on the $a_\phi(675)$ interval. The function is then evaluated at the mid-point of the array, and the half in which the function changes sign becomes the new search interval. In this manner, the solution interval, which will be two adjacent points on the $a_\phi(675)$ array, is determined in 5 iterations. Linear interpolation across the interval yields the semi-analytical $a_\phi(675)$ value, and $a_g(400)$ is determined via either one of the R_{rs}-ratio equations using the modeled value of $a_\phi(675)$. If the function does not change sign across the two outermost values, a switch is made to the empirical, two-wavelength default algorithm.

When compared to an older lookup-table-based method (Carder et al., 1991), the bisection method gave identical solutions to within 5 significant digits for $a_\phi(675)$ and $a_g(400)$, and the code ran in 75% of the time that the lookup-table-based version of the code took.

The algorithm code is written in ANSI C. The program file contains about 300 lines of code and comments. It was developed and tested on a DEC Alpha machine which uses the DEC OSF/1 C Compiler. All of the algorithm parameters listed in Table 1 are read in from a file, so different parameter tables can easily be constructed for different applications. The code is available via anonymous ftp at:

gold.marine.usf.edu locates at /pub/swf_alg/

4.0 Algorithm Evaluation

4.1 Statistical criteria

To evaluate algorithm performance we generated statistics that are determined on log-transformed variables so as to provide equal weighting to data from all parts of the pigment and reflectance ranges. The slope and intercept values are from Type II RMA regressions. The RMS statistic described is based on the root-mean square of the logarithm of the ratio of modeled-to-measured values

(O'Reilly and Maritorena, 1997) and will be referred to here as RMS1. We also generated values for r^2 and root-mean-square error on the non-log-transformed (linear) data. Our RMS statistic will be referred to as RMS2 and is described by

$$RMS2 = \sqrt{\frac{\sum_{i=1}^{n}\left[\frac{x_{mod,i} - x_{obs,i}}{x_{obs,i}}\right]^2}{n-2}} \quad (20)$$

where $x_{mod,i}$ is the modeled value of the *i*th element, $x_{obs,i}$ is the observed (or *in situ* or measured) value of the *i*th element, and n is the number of elements. Note that 10^{RMS1}-1.0 $\approx$ RMS2 if there is no bias between the modeled and measured data.

We used two graphical means of evaluating algorithm performance: scatter plots of modeled versus observed values and quantile-quantile plots (O'Reilly and Maritorena, 1997).

4.2 Tests with USF data (Carder data set)

We initially tested our algorithm with our own data set, called the Carder data set in the Evaluation Data Set chapter (Maritorena et al., 1997). However, the data set we present here differs from the Carder data used in the global evaluation data set in two ways. First, we include observed values of $a_\phi(675)$, and $a_g(400)$ wherever possible to accompany the observed $R_{rs}(\lambda)$ and chl *a*. Second, 17 points of high-chlorophyll, high-scattering stations, mostly from the Mississippi River Plume region, are included. The data sources are listed in Table 2.

$R_{rs}(412)$, $R_{rs}(443)$, $R_{rs}(490)$, $R_{rs}(510)$, and $R_{rs}(555)$ were derived from hyperspectral $R_{rs}(\lambda)$ measurements collected just above the sea surface (for measurement protocols, see Lee et al., 1996) by weighting to simulate the SeaWiFS band responses (Barnes et al., 1994). All chl *a* values were determined fluorometrically (Holm-Hansen and Riemann, 1978). $a_\phi(675)$ was determined as described in Section 3.1.2.3.1. $a_g(400)$ was determined by measuring 0.2 uM filtered seawater in a spectrophotometer.

Algorithm performance was evaluated on both the n=87 subset of stations which correspond to the data available in the SeaBASS evaluation data set provided by Carder and on the full n=104 set. The algorithm parameters used are shown in Table 1. For the n=87 subset, all but one of the points were determined via the semi-analytical portion of the algorithm. chl *a*, $a_\phi(675)$, and $a_g(400)$ were predicted with RMS1 errors of 0.122, 0.131, and 0.252, respectively, and RMS2 errors of 0.289, 0.302, and 0.405, respectively. All of the statistics for this and for all evaluations are shown in Table 4. The results are

shown as scatter (Figure 6a) and quantile (Figure 6c) plots. The crosses on the plots are the points determined with the semi-analytical blended algorithm, and all but 4 of these points are from the n=87 data set. The chl *a* and $a_\phi(675)$ data appear to be quite evenly clustered about the one-to-one line on both scatter and quantile plots with no tails at either end. The $a_g(400)$ points are predominantly below the one-to-one line and show a very low bias. There are only 26 points in this plot because measured values of $a_g(400)$ are infrequently available for comparison.

4 of the 17 additional high-chlorophyll points are determined by either the semi-analytical or blended portion of the algorithm. chl *a* values for the other 13 points are thus determined by the default empirical algorithm. However, since the default portion of the algorithm does not yet return values for $a_\phi(675)$ and $a_g(400)$, these high-chlorophyll points add little to the tests for those variables. The RMS1 and RMS2 errors for chl *a* for this composite data set were 0.132 and 0.300, respectively. The results are also shown in Figure 6a and 6c (diamonds). The additional high-chlorophyll points extend nicely along the one-to-one line on both the scatter and quantile plots.

4.3 Tests using a global data set

A large (n=919) global evaluation data set consisting of measured R_{rs} values at the SeaWiFS wavelengths and pigment measurements was collected by the NASA SeaWiFS Project for the SeaBAM algorithm intercomparison exercise (Maritorena et al., 1997). These data came from various researchers around the U.S. and Europe. There were no observed (*in situ*) values of $a_\phi(675)$ or $a_g(400)$ provided in this data set. In addition to these data, we have received 36 data points from the equatorial Pacific, which consisted of R_{rs} measurements made above the surface (EqPac, courtesy of C. Davis), and we collected additional data sets from the Southern California Bight (04/97 with G. Mitchell), near Hawaii (02/97 with D. Clark), and the Kuroshio edge of the E. China Sea (05/97 with G. Gong). An additional SeaBAM data set provided EqPac Rrs determinations from below water for algorithm comparisons for both methods. The SCB data provided an opportunity to measure above-water Rrs and to measure phytoplankton absorption spectra for conditioning absorption parameters for a region exhibiting higher

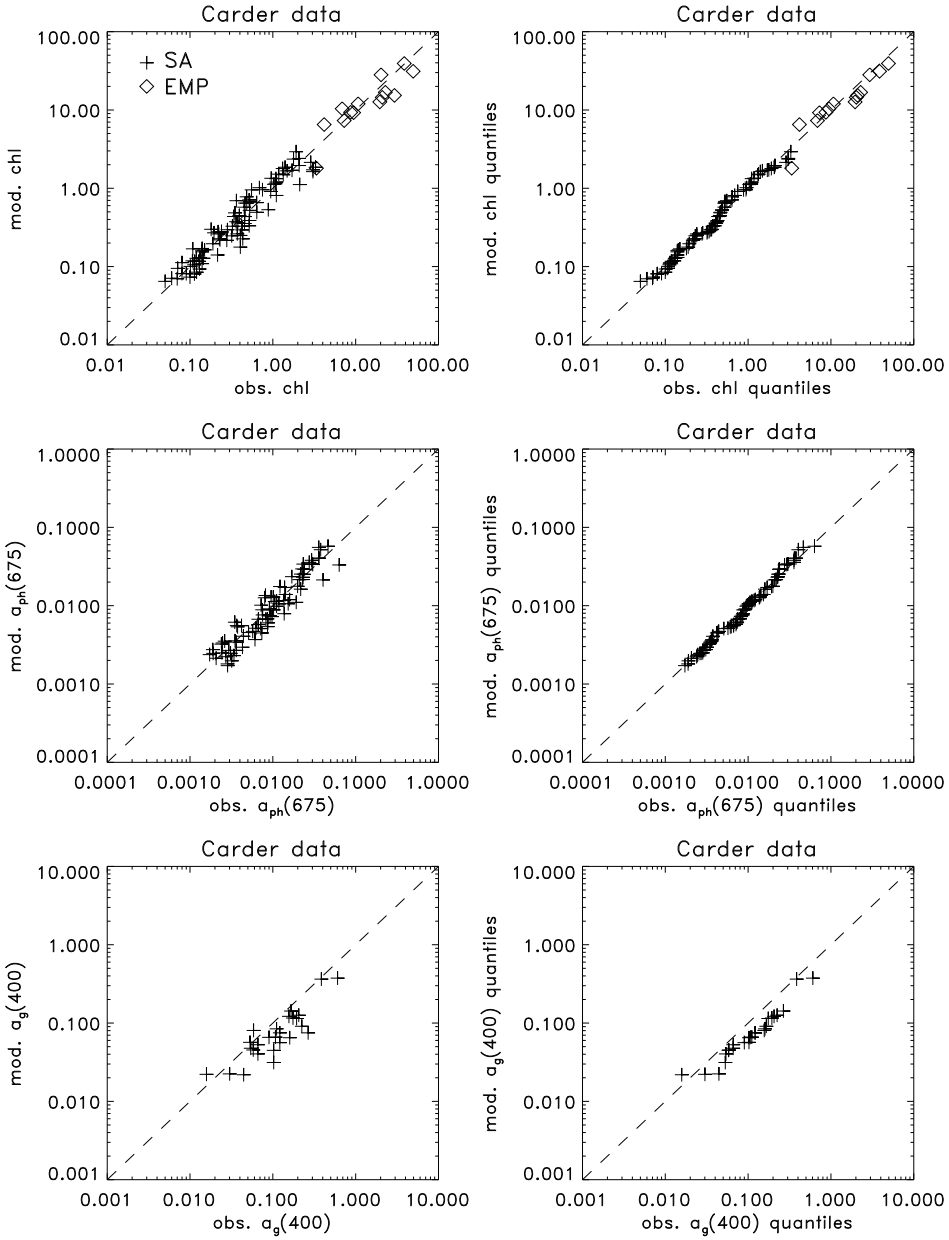

Figure 6. Algorithm performance for Carder data set. Top panels are observed vs. modeled chl *a*, middle panels are observed vs. modeled $a_{ph}(675)$, and bottom panels are observed vs. modeled $a_g(400)$. Left panels are scatter plots and right panels are quantile-quantile plots. The lines are the one-to-one lines in all panels. SA (cross) indicates points which are calculated semi-analytically or by a blend of semi-analytical and empirical values. EMP (diamond) indicates points that are calculated empirically.

levels of pigment packaging than do our subtropical stations. This "packaged" parameterization is used for modelling the multi-year CalCOFI data set of subsurface Rrs values provided to the SeaWiFS data archive by G. Mitchell. The Hawaiian and E.China Sea data sets provided additional oligotrophic data and data from the planned prime site for vicarious calibration for both SeaWiFS and MODIS.

Since many different locations and sensors were involved with the global data collection, and as many as four separate sensor channels must be well calibrated to provide accurate spectral ratios of R_{rs}, an attempt was made to select an initial core set of data consistent with Case 1 waters and with each other. Also, an attempt was made to partition the data sets into one for regions where little pigment packaging is to be expected (e.g., high-light, non-upwelling locations in warm, tropical and subtropical waters), and one where more packaging might be expected (e.g., western boundary upwelling, non-summer, high latitude, etc.). To help in this task, the data were examined with the help of two numerical filters.

The first numerical filter developed was to compare the data sets with the CZCS chlorophyll pigment algorithm ($C = 1.14\ [r_{25}]^{-1.71}$, $r_{25} = R_{rs}(443)/R_{rs}(555)$) to check for consistency with this classical algorithm for Case 1 waters. Figures 7d, 8d, and 9d show scatter-plots of observed chl *a* versus r_{25} for different groups of data, with the CZCS algorithm illustrated by the dotted line. The warm-water, subtropical and tropical data sets (Figure 7d) were mostly consistent with the CZCS algorithm for pigment values less than about 1 mg m^{-3}. When data from eastern boundary and upwelling locations (Figure 7c) were applied to the CZCS algorithm, however, they provided chlorophyll *a* values typically 50% to 90% lower than measured, suggesting that perhaps regional algorithms are needed to obtain best results for such waters. This helped separate the data into two water types, which we will call "unpackaged"-pigment waters and "packaged"-pigment waters. Since this "packaging" filter is not applicable using only spacecraft-derived data, a second type of packaging filter was sought.

A second numerical filter was developed using the ratios r_{12} (= $R_{rs}(412)/R_{rs}(443)$) and r_{25} (Figures 7b and 8b). For waters with unpackaged pigments, the line $r_{12} = 0.95\ [r_{25}]^{0.16}$ was used to separate high-gelbstoff data points (those below the line in Figures 7b, 7b) from the Case 1 data. Based upon the Carder a_g data, the gelbstoff-rich Case 2 data had $a_g(400)$ values typically in excess of the relationship $0.12\ [\text{chl } a]^{0.7}$, where 0.12 has the units m^2 (mg chl)$^{-1}$. Since this data set contained both gelbstoff and chlorophyll a measurements and had been acquired by making R_{rs} measurements against a reflectance standard, minimizing calibration uncertainties (see Carder and Steward, 1985), it was used to evaluate tropical and subtropical waters for gelbstoff-rich conditions, to identify data sets with more packaging, and to flag data sets with possible sensor-calibration uncertainties.

To learn to identify waters with more packaged pigments using remotely sensed data, Case 1 data from a traditional upwelling region (e.g., CalCOFI) were examined. These data are shown in Figure 8b for comparison to the unpackaged data of Figure 7b. Since pigment packaging reduces the absorption for a given concentration of pigments far more at 443 nm than at 555 nm, and somewhat more at 443 nm than at 412 nm, packaging significantly reduces r_{25} while increasing the r_{12} ratio somewhat. This, then places packaged data points below the $r_{12} = 0.95\ [r_{25}\ ]^{0.16}$ line even without excessive gelbstoff concentrations (Fig. 7b), at least for points with r_{25} values in excess of a value of about 3.0.

For us to be certain that the numerical filter approach works consistently at separating even more heavily packaged data sets from unpackaged ones, more data sets need to be evaluated. Measurements of particulate and detrital absorption would be useful. A nascent outline of an approach to vary algorithm parameters using measurements from space is suggested by our work with the r_{12} vs. r_{25} numerical filter. This approach will be supplemented with a temperature-anomaly approach based upon estimating regions experiencing nutrient-replete conditions (Kamykowski 1987). This should improve our facility and accuracy in modulating the pigment-absorption parameters for future ocean-color algorithms.

4.4 Algorithm evaluation with the "unpackaged" data set

Those data sets generally found consistent with the CZCS algorithm line as well as occurring above the line $r_{12} = 0.95\ [r_{25}]^{0.16}$ for points where $r_{25} > 3.0$, were classified as “unpackaged”, in reference to the pigment effects on the optics prevalent at those locations at the time of data collection. There are 287 data points in this ensemble data set: 134 USF data points and 37 EqPac equatorial Pacific points, all measured above-surface and processed using the Lee et al. (1996) protocols, and 126 EqPac points, all measured below-surface using the Mueller and Austin (1995) protocols. Of these points, 261 (91%) were processed by the semi-analytical portion of the algorithm yielding RMS1 and RMS2 errors of 0.099 and 0.230, respectively. The scatter (Figure 7a) and quantile (Figure 7b) plots overlay the one-to-one line at the ends as well as in the middle. For the log-transformed variables, the Type II RMA slope was 0.999, the bias was 0.002, and r^2 was 0.873. When all 287 data points were considered using the semi-analytical algorithm plus the blended and empirical algorithms, RMS1 and RMS2 errors were 0.108 and 0.242, respectively. The Type II RMA slope and intercept was 0.973, the bias was -0.003, and r^2 was 0.955. Table 4 has a a complete summary of these statistics. Note that since these algorithms are largely semi-analytical in nature and were generated using mostly Gulf-of-Mexico data for the parameterization, one would not expect to always have slope values of 1.000 and bias values of 0.000 as result from empirical regression algorithms fit to a single data set. Note also that the r^2 values increased using the

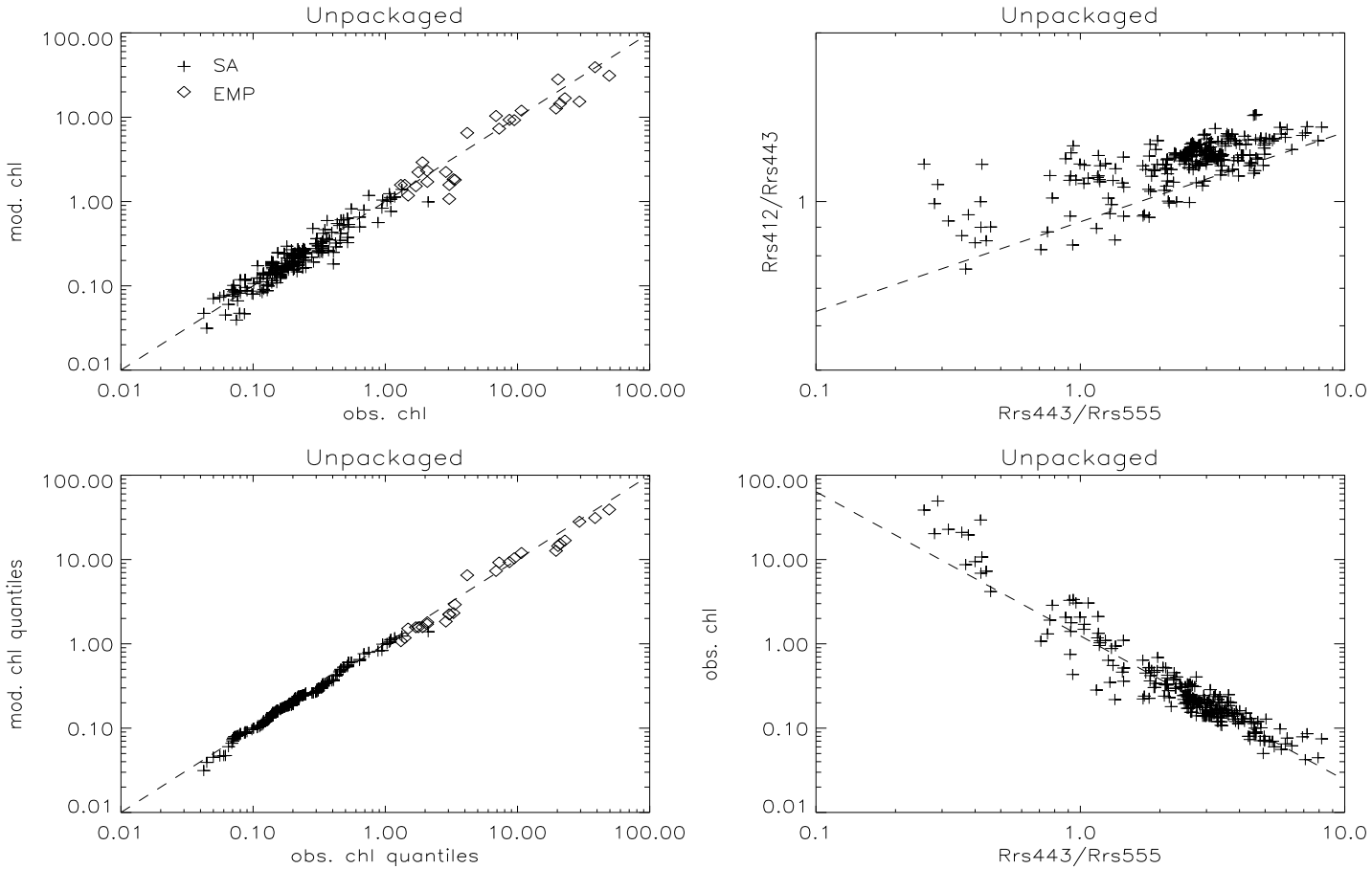

Figure 7. Algorithm performance for and analysis of data sets passing the "unpackaged" numerical filter. Top left panel, a) scatter plot of observed vs. modeled chl *a* (mg m^{-3}). The dashed line is the one-to-one line. Bottom left panel, c) quantile-quantile plot of observed vs. modeled chl *a*. Top right panel, b) r_{12} vs. r_{25}, with the line, $r_{12} = 0.95[r_{25}]^{0.16}$, used to identify "unpackaged" Case 1 data (above line). Bottom right panel, d) observed chl *a* vs. r_{25}, with the CZCS algorithm line $C = 1.14[r_{25}]^{-1.71}$.

blended algorithm because of the extended range of chlorophyll *a*. RMS2 errors of less than 25% exceed our accuracy goal of 35% or less.

4.5 Algorithm evaluation with the "packaged" data set

Several data sets within the global evaluation set were numerically diagnosed as coming from waters where the pigments were much more "packaged" than those from the warm, tropical and subtropical data sets evaluated earlier. The other data sets in the archive appeared to contain perhaps both packaged and unpackaged data. Simulations of the optical properties for these regions required some minor alterations of the phytoplankton absorption characteristics, based upon the decreased specific absorption values observed in the California Current area during the CalCOFI 9704 cruise. The new parameters, shown in Table 3, are used to define a slightly different, "packaged" algorithm.

There are 326 points in an ensemble of multi-year data sets from the California Current which we label as "packaged." These consist of CalCOFI (n=303) and Cal9704 (n=23) data which we recently collected with G. Mitchell. The CalCOFI data were subsurface while the Cal9704 data were above-surface collections. 303 points (93%) from this "packaged" data set passed the semi-analytical portion of the new algorithm, yielding RMS1 and RMS2 errors for chl *a* retrieval of 0.111 and 0.268, respectively. The Type II RMA slope and intercept was 0.999, the bias was -0.006, and r^2 value was 0.917. The scatter plot (Figure 8a) overlays the one-to-one line and the quantile plot (Figure 8b) is linear and overlies the line, but has a slight discountinuity near a chlorophyll value of 3. Using the blended algorithm on 326 data points, the r^2 increased to 0.951 while the other statistics remained about the same (Table 4). RMS2 errors of about 28% also exceeds our accuracy goal of 35% or less

4.6 Algorithm evaluation with a global data set

To generate an algorithm to transition from regions and periods with packaged and unpackaged pigments, we developed a global data set combining the "packaged", "unpackaged", and other mixed data sets from SeaBAM. This data set has 976 data points. We then developed a set of compromise parameters for this "global" average algorithm, shown in Table 3, for use at times and places where "packaging" is unknown or transitional. For this data set and these "average" parameters, 883 points (90.5%) of the points passed the semi-analytical portion of the algorithm, yielding RMS1 and RMS2 errors in algorithm-derived chl *a* of 0.176 and 0.446, respectively. The Type II RMA slope was 1.003, the bias was 0.002, and r^2 was 0852. Statistics for the entire n=976 set were similar except r^2 was higher (0.913). The scatter plot (Figure 9a) looks evenly clustered about the one-to-one line and the quantile

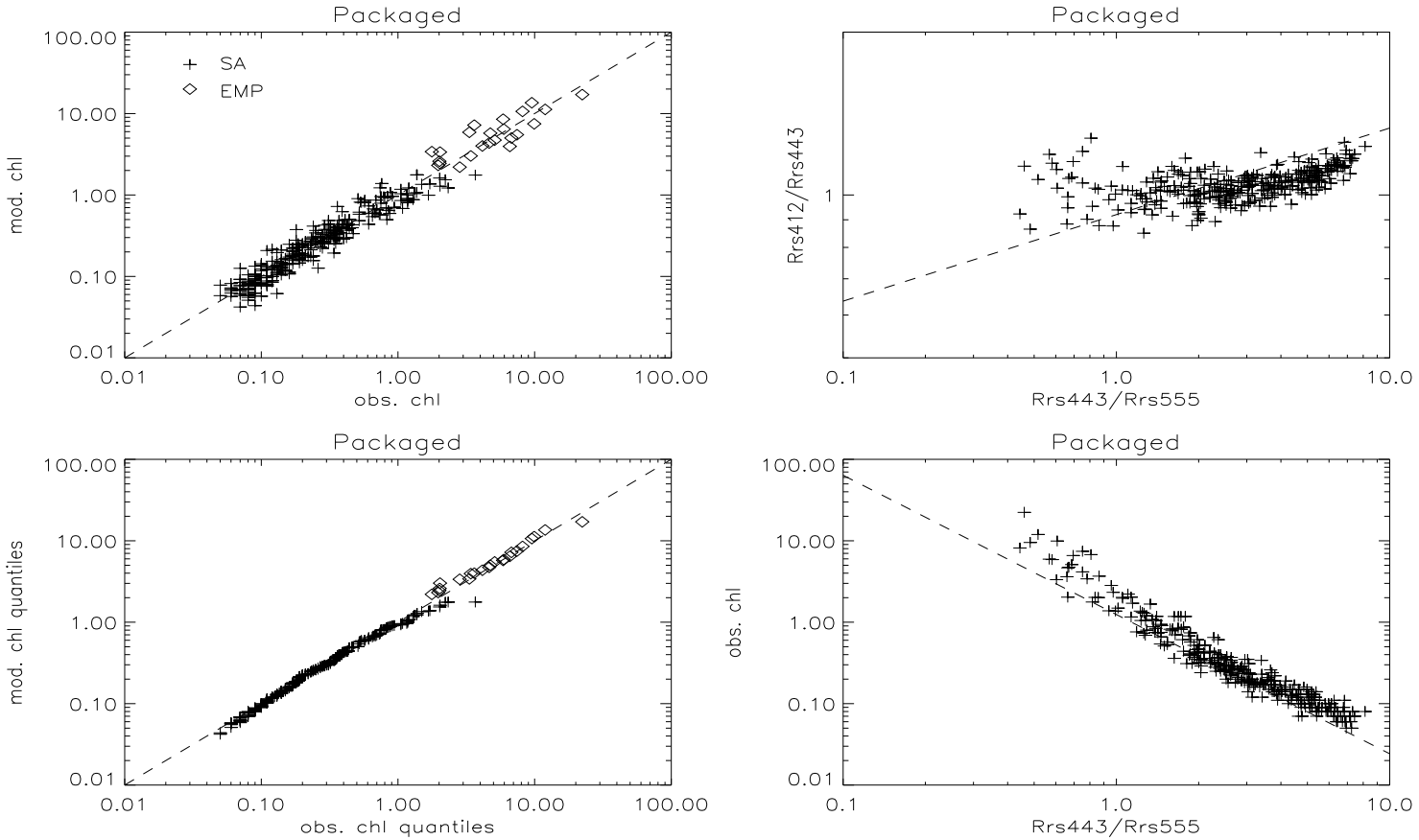

Figure 8. Algorithm performance for and analysis of data sets passing the "packaged" numerical filter. Top left panel, a) scatter plot of observed vs. modeled chl *a* (mg m^{-3}). The dashed line is the one-to-one line. Bottom left panel, c) quantile-quantile plot of observed vs. modeled chl *a*. Top right panel, b) r_{12} vs. r_{25}, with the line, $r_{12} = 0.95[r_{25}]^{0.16}$, used to identify "unpackaged" Case 1 data (above line). Bottom right panel, d) observed chl *a* vs. r_{25}, with the CZCS algorithm line $C = 1.14[r_{25}]^{-1.71}$.

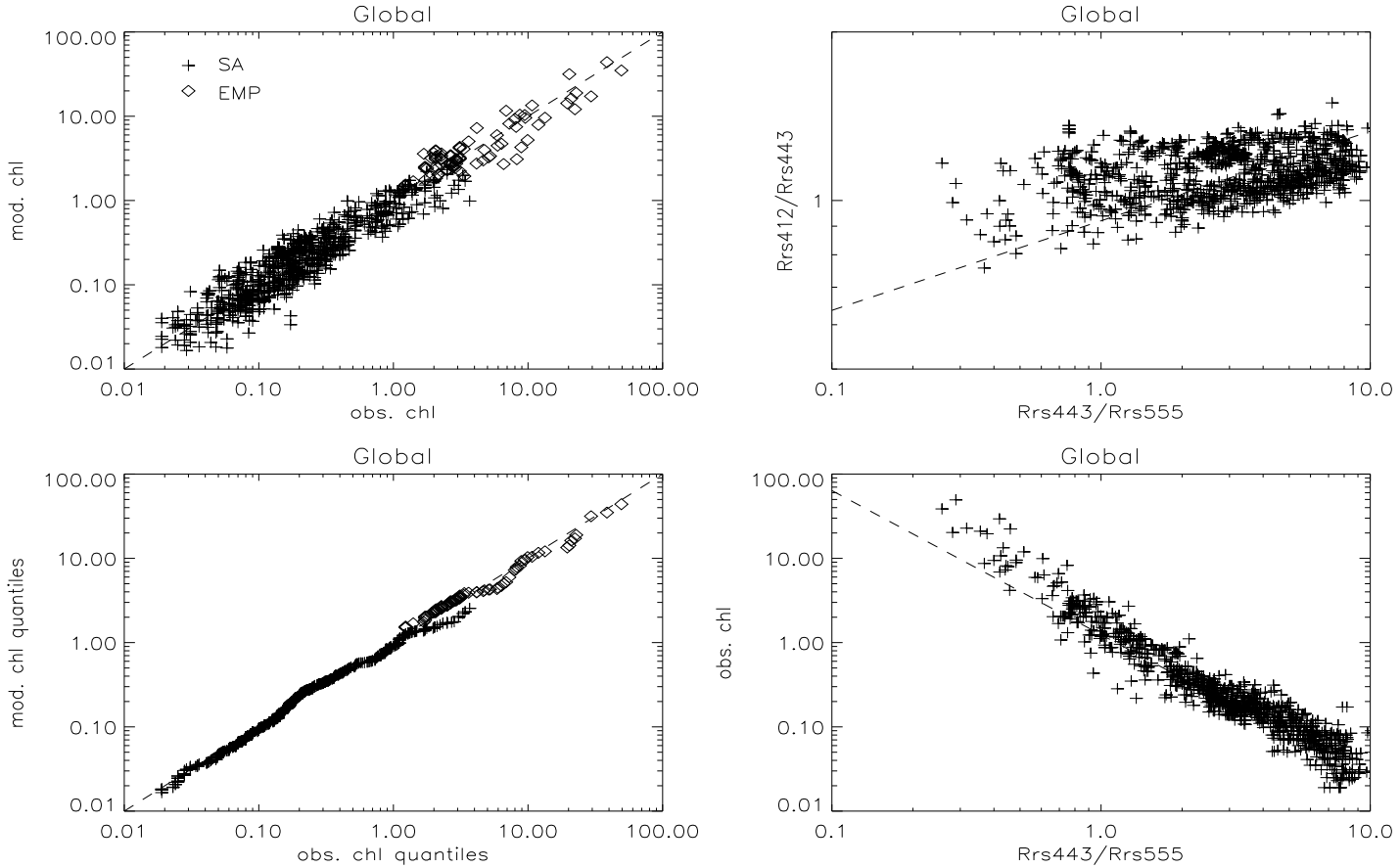

Figure 9. Algorithm performance for and analysis of global data sets without partitioning into "packaged" or "unpackaged" subsets. Top left panel, a) scatter plot of observed vs. modeled chl *a* (mg m^{-3}). The dashed line is the one-to-one line. Bottom left panel, c) quantile-quantile plot of observed vs. modeled chl *a*. Top right panel, b) r_{12} vs. r_{25}, with the line, $r_{12} = 0.95[r_{25}]^{0.16}$, used to identify "unpackaged" Case 1 data (above line). Bottom right panel, d) observed chl *a* vs. r_{25}, with the CZCS algorithm line $C = 1.14[r_{25}]^{-1.71}$.

plot (Figure 9b), though wiggly, overlays the one-to-one line for the most part. Note that if we are unable to accurately specify the packaging domains of the world ocean, a compromise, blobal algorithm with about 44% accuracy is likely to be the best accuracy that we can achieve.

5.0 Discussion

The biggest limitation to algorithm development for the global ocean is a paucity of bio-optical field data from around the globe that are complete with ancillary particle and gelbstoff absorption spectra. These data are needed in order to assess the spatial and temporal variation in the key algorithm parameters X, Y, S, $a_g(400)$, and most importantly, $a_0(\lambda)$ and $a_1(\lambda)$. In order to derive chl *a*, it is vitally important to be able to predict how $a_\phi^*(\lambda)$ will vary. Thus, we must study the effect of light history, which is related to season, cloudiness, latitude, and nutrient history, which is influenced by mixed-layer depth, upwelling, river plumes, and offshore/onshore proximity.

5.1 High b_b pixels

Since the R_{rs} model does not specifically account for absorption and backscattering from suspended sediments or coccolithophores or for reflection from the bottom, a method is needed to determine which pixels are influenced by any of these. Such waters will be referred to as "high-b_b Case 2" waters, as opposed to high-gelbstoff Case 2 waters, which the model explicitly accounts for. Although not yet implemented, a possible means of identifying high-b_b Case 2 stations is to examine the $R_{rs}(670):R_{rs}(555)$ ratio. Retaining $b_b(\lambda)$ in the denominator of Eq. 1 is required, and the site-specific behavior of sediment absorption characteristics must be known. A new spectral, backscatter-coefficient meter is now commercially available and will help with X and Y parameterization.

5.2 a_ϕ in other environments

We have learned from trends in the data observed so far that the unpackaged, semi-analytical algorithm performs as well with temperate summer data (TT010 north of 45^0 and MLML 2 north of 50^0) as it does with subtropical data for all seasons. How, then, might temperate data from other seasons and/or data from upwelling and high-latitude areas differ from the temperate summer, non-upwelling data?

To initially address this question we compare $a_\phi(\lambda)$ data from MLML 1 (May, 50^0–60^0 N), MLML 2 (August, 50^0–60^0 N), TT010 (July, north of 45^0), Monterey Bay (fall, upwelling region), and 2 coastal upwelling stations from the Arabian Sea. Although the Arabian Sea data points were collected

from a subtropical summer (June) environment, the water was about 4 ^{0}C cooler than offshore waters, indicating a lower-light, nutrient-rich, upwelling source, conditioning the water for highly packaged, fast-growing species such as diatoms. This is manifest in Figure 10, where these data fall among the more packaged points. Here, the ratios of the blue peak to the red peak, $a_\phi(443):a_\phi(675)$, are plotted as a function of the height of the red peak itself, $a_\phi(675)$, which can be thought of as an indicator of pigment concentration. The subtropical algorithm values (solid line) and trend lines for the high and low outlying points for the entire data set (dashed lines) are also shown. The dotted line represents a median trend for the entire Carder data set, and it approximates the mean line for two years of data from the Southern California Bight (SCB) (B. G. Mitchell, personal communication). The SCB data also ranged widely between the top and bottom dashed curves.

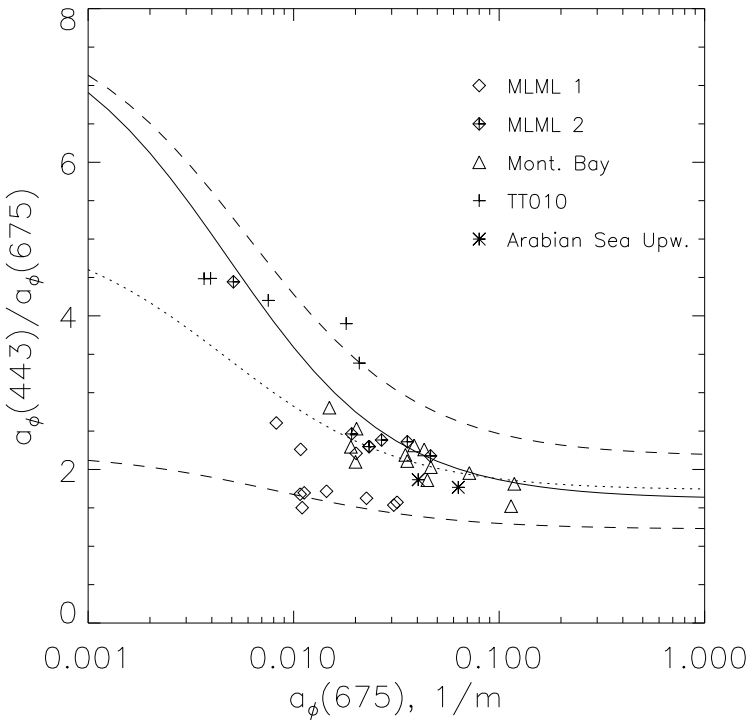

Figure 10. $a_\phi(443)/a_\phi(675)$ vs. $a_\phi(675)$ for stations from various non-subtropical environments. The solid line is the function used in the "unpackaged" semi-analytical algorithm. The dashed lines represent the lower and upper bounds for all of the absorption ratio data that we have collected (not shown) and the dotted line approximates the median trend.

The first thing to note in Figure 10 is how well the subtropical line is followed by the high-latitude summer data. In fact, two of the summer TT010 points along the Washington coast fall among the highest of the subtropical data. The phaeocystis-rich, spring-bloom, MLML 1 data, however, represent data with the lowest specific absorption coefficients of the entire study. Similarly, upwelling data from the Arabian Sea and Monterey Bay fall below the median line for the data set. These data trends suggest that there is less packaging in summer temperate data than at other times. Maximal packaging appears associated with high-latitude, low-light, spring bloom stations (MLML 1) and with typically cloudy upwelling sites. The data also suggest that, as we saw in Section 4, a single global algorithm will lack the accuracy needed to address data sets that include subtropical, high-latitude, and upwelling areas. For the non-subtropical areas, some of the parameters in Table 2 may need to be functions of region and season.

6.0 A Strategy for Implementation of Variable Package Parameters

While algorithms appropriate for regions with packaged or unpackaged pigments can reduce the uncertainty in chlorophyll-a concentration from perhaps 50% to less than 30%, methods to determine when and where to apply appropriate parameterization based upon space-derived data are still under development. A numerical filter approach has already been discussed, but it is only useful for oligotrophic waters where $r_{25} > 3.0$, and high gelbstoff concentrations cause confusion. This approach needs to be compared and augmented by at least one other method. A second approach uses the fact that unpackaged pigments are usually found in high-light, nutrient-poor waters where small-diameter phytoplankton cells predominate (e.g. Herbland et al. 1984; Carder et al. 1986). Since dissolved nutrients cannot be detected from space, a nutrient surrogate was sought.

Kamykowski (1987) developed a model that explained much of the covariance observed between upper-layer temperature and nitrate concentrations (e.g. Zentara and Kamykowski, 1977; Kamykowski and Zentara, 1986). Kamykowski (personal communication) has since developed nitrate-depletion temperatures (NDTs) for the global ocean. These NDTs provide a means to observe from space a variable that indicates when and where nitrate may be limiting phytoplankton growth, and where upper-layer production is dependent upon recycled nitrogen. Such phytoplankton are typically small (Herbland et al., 1984) with unpackaged pigments (Carder et al., 1986).

To delimit regions with pigments without self-shading or packaging, we propose to compare monthly sea-surface temperatures to Kamykowski's NDTs. Figure 11 shows annual trends in sea-surface temperature (SST), chlorophyll a [Chl a], and NDTs for the Gulf of Maine, Bermuda, and

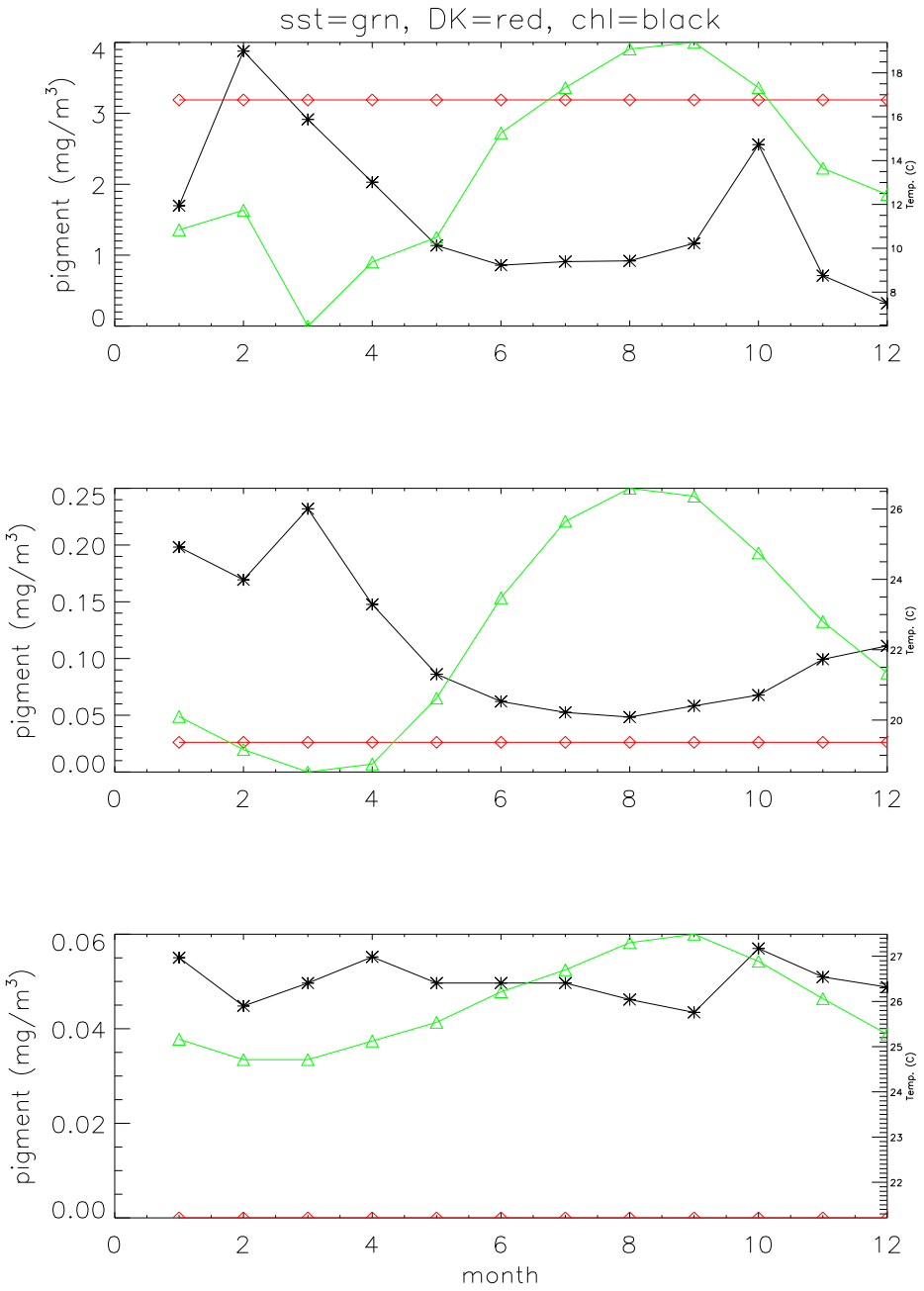

Figure 11. Four-year (1982-1985), monthly-mean values of sea-surface temperature (triangles), CZCS pigment (asterisks), and nitrate-depletion temperature (diamonds) for locations near a) the Gulf of Maine, b) Bermuda, and c) Barbados.

Barbados. The temperatures and pigments are four-year (1982-85) monthly averages from the AVHRR and CZCS sensors (USA_NASA_JPL_PODAAC_A005). Note that by this approach, pigments in the Gulf of Maine are rarely designated as being unpackaged, those near Barbados are always designated as being unpackaged, while those near Bermuda are designated as being unpackaged in the summer and packaged in the winter-spring.

Clearly the Gulf of Maine is a lower-light and higher-nitrate environment than are Bermuda waters, so the degree of packaging there is likely to be much higher. To indicate a higher degree of packaging, we propose a "packaged" temperature range, SST_p < NDT - 0.5°C, below which packaging is significant. For waters with pigments expected to have little or no packaging, we propose an "unpackaged" temperature range, SST_u > NDT + 1.0°C. For pixels falling in either of these two ranges the semi-analytical algorithm will use the "packaged" and "unpackaged" pigment-absorption parameters, respectively. For waters with temperatures between SST_p and SST_u the parameters will be set to the "global" values (see Table 3). The regions of the north Atlantic Ocean falling within each of these domains is shown in Figs. 12 and 13 for April and August, respectively.

This approach will be tested using the SeaBASS bio-optical data base. Initially, we will use historical, monthly climatological values of SST to partition the data into three regimes to simulate pigment packaging. The algorithm will be tested and the results used to adjust SST_p and SST_u boundary values. We expect these values to differ for spring-summer transitions compared to summer-fall transitions due to the different seed populations available to initiate fall blooms relative to spring blooms. More definitive evaluations of algorithm performance can be made once actual SST values are provided in bio-optical data sets.

We expect that this approach -- partitioning space-derived ocean-color data into bio-optical regimes that reflect natural changes in pigment packaging -- can improve algorithm performance from a best of about +/- 50% to better than +/- 30%. Without such partitioning, meeting the MODIS ocean-team goal of providing chlorophyll-a concentrations with accuracies of 35% or better is unlikely.

7.0 Conclusions

A semi-analytical algorithm was tested with a total of 604 points from regions where the pigments were typically unpackaged- or packaged, with appropriate algorithm parameters for each data type. The "unpackaged" type consisted of data sets that were generally consistent with the Case 1 CZCS algorithm and using well calibrated data sets. The "packaged" type consisted of data sets apparently containing somewhat more packaged pigments, requiring modification of the absorption parameters of

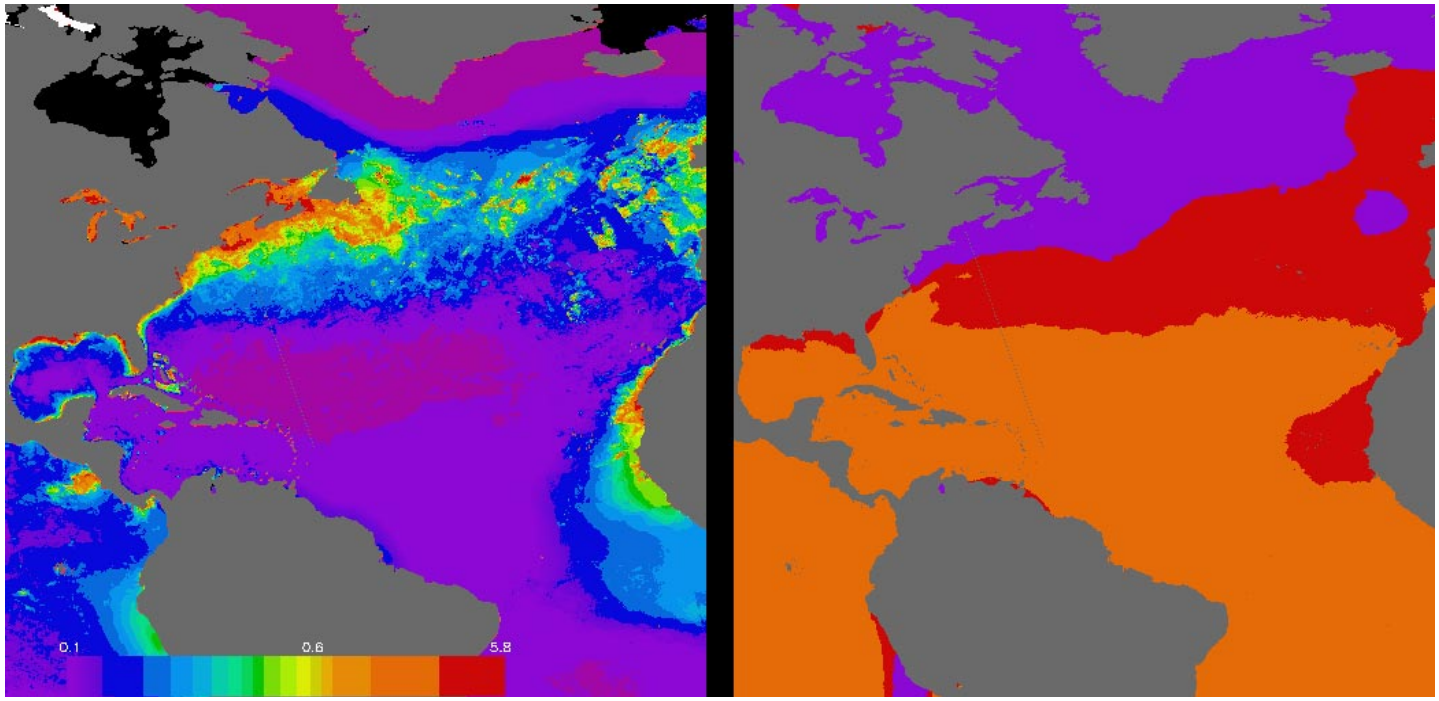

Figure 12. Mean (1982-1985), April, CZCS-pigment concentrations for the north Atlantic Ocean (a) and pigment-packaging regimes for April (b). The purple region in (b) represents the packaged bio-optical domain, orange represents the unpackaged, and red-orange represents the transitional domain, while the "pink" to red-orange regions in (a) transition from 0.04 to > 4.0 mg-m^{-3} concentrations of CZCS pigment.

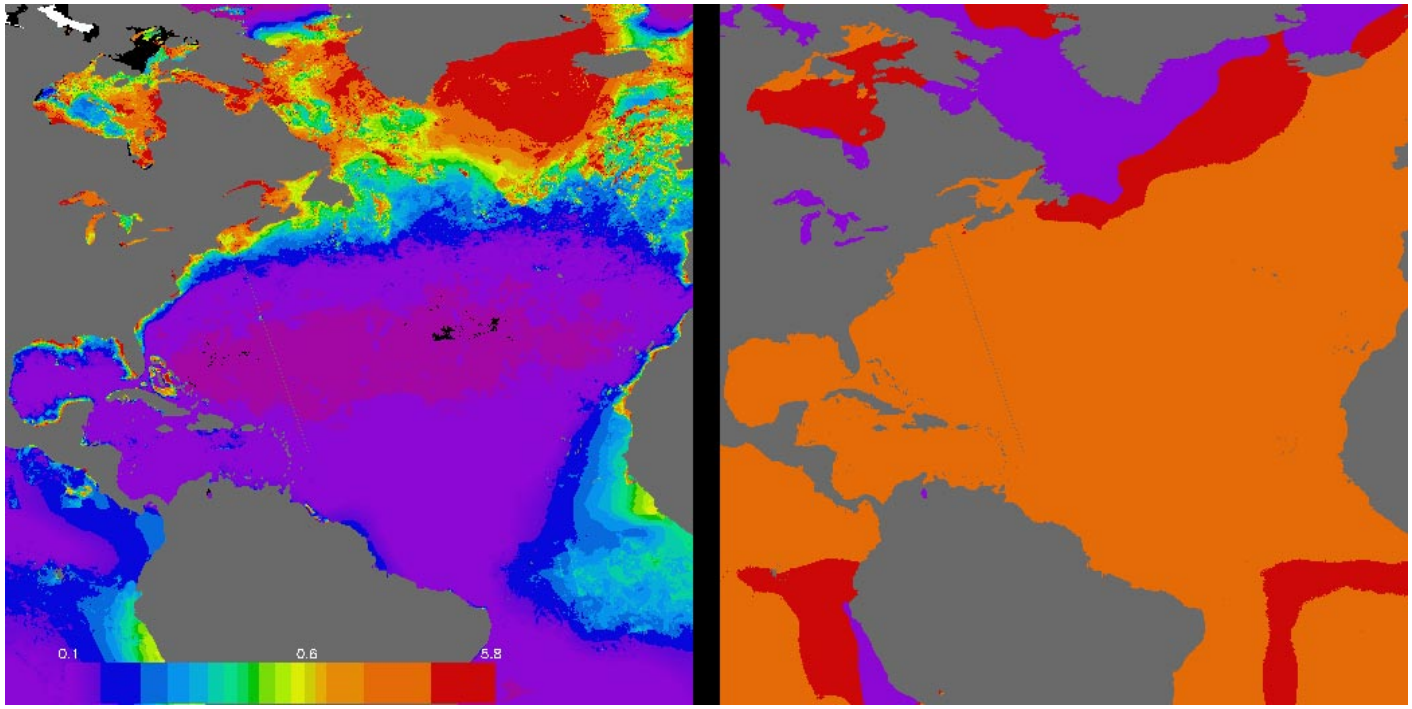

Figure 13. Mean (1982-1985), August, CZCS-pigment concentrations for the north Atlantic Ocean (a) and pigment-packaging regimes for August (b). The purple region in (b) represents the packaged bio-optical domain, orange represents the unpackaged, and red-orange represents the transitional domain, while the "pink" to red-orange regions in (a) transition from 0.04 to > 1 mg-m^{-3} concentrations of CZCS pigment.

the semianalytical model consistent with the CalCOFI study area. This resulted in two fairly equally divided data sets.

The semi-analytical algorithm performed superbly on each of the data sets after classification, resulting in RMS1 errors of 0.102 and 0.111 (e.g. 1/10 log units), respectively, for the unpackaged and packaged data-set classes, with little bias and slopes near 1.0. In combination, the RMS1 performance was 0.110. RMS2 errors for the algorithms were 24% and 28%, respectively.

While these numbers appear rather sterling, one must bear in mind what misclassification does to the results. Using an average or compromise parameterization on the modified global data set yielded an RMS1 error of 0.174, while using the unpackaged parameterization on the global evaluation data set yielded an RMS1 error of 0.284. So, without classification, the algorithm performs better globally using the average parameters than it does using the unpackaged parameters. Some 372 data points in the the Sea BASS archive were from data sets that were mixed or transitional between "packaged" or "unpackaged" data types, not clearly falling into packaged or unpackaged classes without more information (e.g. the BATS data from near Bermuda contained both classes). Given locations and temperatures, we propose to use nitrogen-depletion temperatures to sort these data into appropriate classes of packaging on a monthly basis and reprocess the transitional data sets.

8.0 Output Products

Output products from MOD-19 will include the following:

1. Concentration of chlorophyll *a* for concentrations from .02 to 50 mg/m^3 for optically deep waters.

2. The absorption coefficient at 400 nm , $a_g(400)$ due to gelbstoff or colored, dissolved organic matter. All absorption coefficients $a_g(\lambda)$ for $400 \leq \lambda \leq 700$ nm can then be estimated with knowledge of the spectral slope parameter S.

3. The absorption coefficient at 443 nm, $a_\phi(443)$, due to phytoplankton; this is passed along to MOD-20 for calculation of $a_\phi(\lambda)$ for the visible spectrum as a contribution to the absorbed radiation by phytoplankton, ARP, used for fluorescence efficiency calculations.

4. The sum of $a_w(\lambda)$, $a_g(\lambda)$, and $a_\phi(\lambda)$ provides the total absorption coefficient spectrum, $a_t(\lambda)$, and the diffuse attenuation spectrum, $k_d(\lambda) = a_t(\lambda) / \cos \theta_0$. See MOD-20.

9.0 References

Aiken, J., G. F. Moore, C. C. Trees, S. B. Hooker, and D. K. Clark, The SeaWiFS CZCS-type pigment algorithm, in *SeaWiFS Technical Report Series,* S. B. Hooker and E. R. Firestone, eds., Vol. 29, 1995.

Austin, R. W., Inherent spectral radiance signals of the ocean surface, in *Ocean Color Analysis, SIO ref. 74–10*, pp. 2.1–2.20, Scripps Inst. of Oceanogr., La Jolla, Calif, 1974.

Baker, K. S., and R. C. Smith, Bio-optical classification and model of natural waters 2, *Limnol. Oceanogr.*, 27, 500–509, 1982.

Barnes, R. A., W. L. Barnes, W. E. Esaias, and C. R. McClain, Prelaunch acceptance report for the SeaWiFS radiometer, in *SeaWiFS Technical Report Series,* S. B. Hooker, E. R. Firestone, and J. G. Acker, eds., Vol. 22, 1994.

Bricaud, A., A. Morel, and L. Prieur, Absorption by dissolved organic matter in the sea (yellow substance) in the UV and visible domains, *Limnol. Oceanogr.*, 26, 43–53, 1981.

Carder, K. L., and R. G. Steward, A remote-sensing reflectance model of a red tide dinoflagellate off West Florida, *Limnol. Oceanogr.*, 30, 286–298, 1985.

Carder, K. L., R. G. Steward, G. R. Harvey, and P. B. Ortner, Marine humic and fulvic acids: Their effects on remote sensing of ocean chlorophyll, *Limnol. Oceanogr*., 34, 68–81, 1989.

Carder, K. L., S. K. Hawes, K. A. Baker, R. C. Smith, R. G. Steward, and B. G. Mitchell, Reflectance model for quantifying chlorophyll *a* in the presence of productivity degradation products, *J. Geophys. Res.*, 96(C11), 20,599–20,611, 1991.

Carder, K. L., S. K. Hawes, and Z. Lee, MODIS Ocean Science Team ATBD, Case 2 Chlorophyll *a*, 1996.

Carder, K. L., S. K. Hawes, and Z. Lee, SeaWiFS algorithm for chlorophyll *a* and colored dissolved organic matter in subtropical environments, submitted to *JGR*, 1997.

Jeffery, S. W. and G. F. Humphrey, New Spectrophotometric Egautions for Determing Chlorophylls a, b, c_1, c_2 in High Plants, Alge and Natural Phytoplankton, *Biochim. Physiol. Pflanzen(BPP),* S. 191-194, 1975.

Gong, G.-C., K.-K. Liu, and S.-U. Pai, Prediction of nitrate concentration from two end member mixing in the southern East China Sea, *Cont. Shelf Res.*, 15(7), 827–842, 1995

Gordon, H. R., O. B. Brown, and M. M. Jacobs, Computed relationships between the inherent and apparent optical properties of a flat homogeneous ocean, *Appl. Opt.*, 14, 417–427, 1975.

Gordon, H. R., O. B. Brown, R. H. Evans, J. W. Brown, R. C. Smith, K. S. Baker, and D. K. Clark, A semi-analytic model of ocean color, *J. Geophys. Res.*, 93, 10,909–10,924, 1988.

Gordon, H. R., D. K. Clark, J. W. Brown, O. B. Brown, R. H. Evans, and W. W. Broenkow, Phytoplankton pigment concentrations in the Middle Atlantic Bight: Comparison of ship determinations and CZCS estimates, *Appl. Opt.*, 22, 20–36, 1983.

Gordon, H. R., and A. Y. Morel, *Remote assessment of ocean color for interpretation of satellite visible imagery: A review*, Springer, 1983.

Herbland,A., A. LeBouteiller, and R.Raimbault, Size structure of phytoplankton biomass in the equatorial Atlantic Ocean. *Deep-Sea Res.* 32:819-836, 1985.

Holm-Hansen, O., and B. Riemann, Chlorophyll *a* determination: Improvements in methodology, *Oikos*, 30, 438–437, 1978.

Jerome, J. H., R. P. Bukata, and J. E. Burton, Utilizing the components of vector irradiance to estimate the scalar irradiance in natural waters, *Appl. Opt.*, 27(19), 4012–4018, 1988.

Kamykowski, D., A preliminary biophysical model of the relationship between temperature and plant nutrients in the upper ocean, *Deep Sea Res.*, 34(7), 1067–1079, 1987.

Kamykowski, D., and S.-J. Zentara, Predicting plant nutrient concentrations from temperature and sigma-*t* in the upper kilometer of the world ocean, *Deep Sea Res.*, 33(1), 89–105, 1986.

Kirk, J. T. O., Dependence of relationship between inherent and apparent optical properties of water on solar altitude, *Limnol. Oceanogr.*, 29, 350–356, 1984.

Kirk, J. T. O., Volume scattering function, average cosines, and the underwater light field, *Limnol. Oceanogr.*, 36(3), 455–467, 1991.

Lee, Z., K. L. Carder, S. K. Hawes, R. G. Steward, T. G. Peacock, and C. O. Davis, A model for interpretation of hyperspectral remote-sensing reflectance, *Appl. Opt.*, 33, 5721–5732, 1994.

Lee, Z., K. L. Carder, R. G. Steward, T. G. Peacock, C. O. Davis, and J. L. Mueller, Remote-sensing reflectance and inherent optical properties of oceanic waters derived from above-water measurements, SPIE vol. 2963, 160–166, 1996.

O'Reilly and Maritorena, Maritorena, seabam chapter, 1997.

Mitchell, B. G., Algorithms for determining the absorption coefficients for aquatic particulates using the Quantitative Filter Technique, in *Ocean Optics X*, Proc. SPIE, 1302, 137–148, 1990.

Mitchell, B. G., and O. Holm-Hansen, Bio-optical properties of Antarctic waters: differentiation from temperate ocean models, *Deep Sea Res.*, 38(8–9), 1009–1028, 1991.

Morel, A. Y., and H. R. Gordon, Report of the working group on water color, *Boundary-Layer Meteorology*, 18, 343-355, 1980.

Moore, L. R., R. Goericke, S. W. Chisolm, Comparative physiology of *Synechococcus* and *Prochlorococcus*: influence of light and temperature on growth, pigments, fluorescence and absorptive

properties, *Mar. Ecol. Prog. Ser.*, 116, 259–275, 1995.

Morel, A. Y., and L. Prieur, Analysis of variations in ocean color, *Limnol. Oceanogr.*, 22, 709−722, 1977.

Morel, A. Y, and A. Bricaud, Theoretical results concerning light absorption in a discrete medium and application to the specific absorption of phytoplankton, *Deep Sea Res.*, 28, 1357–1393, 1981.

Morel, A. Y., Optical modeling of the upper ocean in relation to its biogenous matter content (Case 1 waters), *J. Geophys. Res.*, 93, 10,749−10,768, 1988.

Morel, A. Y., and B. Gentili, Diffuse reflectance of oceanic waters: its dependence on Sun angle as influenced by the molecular scattering contribution, *Appl. Opt.*, 30(30), 4427–4438, 1991.

Morel, A. Y., and B. Gentili, Diffuse reflectance of oceanic waters II. Bi-directional aspects, *Appl. Opt.*, 32(33), 6864–6879, 1993.

Morel,A., Ahn, Yu-Hwan, Partensky,F., Vaulot,D., Claustre,H., *Prochlorococcus* and *Synechococcus*: a comparative study of their optical properties in relation to their size and pigmentation. *J. of Mar. Res*., 51, 617-649, 1993.

Morel, A. Y., and B. Gentili, Diffuse reflectance of oceanic waters. III. Implication of bi-directionality for the remote sensing problem, *Appl. Opt.*, 35(24), 4850–4862, 1996.

Mueller, J. L., and R. W. Austin, Ocean optics protocols for SeaWiFS validation, revision 1, *NASA Tech. Memo. 104566*, vol. 25, 1995.

Nelson, J. R., and C. Y. Robertson, Detrital spectral absorption: Laboratory studies of visible light effects on phytodetritus absorption, bacterial spectral signal, and comparison to field measurements, *J. Marine Res.*, 51, 181–207, 1993.

Peacock, T. P., K. L. Carder, and R. G. Steward, Components of spectral attenuation for an offshore jet in the Coastal Transition Zone, *Eos Trans. AGU*, 69, 1125, 1988.

Peacock, T. G., K. L. Carder, P. G. Coble, Z. P. Lee, and S. K. Hawes, Long-path spectrophotometer for measuring gelbstoff absorption in clear waters, *EOS, Trans., AGU*, 75(3), pp. 22, 1994/supplement.

Pope, R. M., and E. S. Fry, Absorption spectrum (380–700 nm) of pure water: II. Integrating cavity measurements, submitted to *Appl. Opt.* March 1997.

Roesler, C. S., M. J. Perry, and K. L. Carder, Modeling *in situ* phytoplankton absorption from total absorption spectra in productive inland marine waters, *Limnol. Oceanogr.*, 34, 1510–1523, 1989.

Shibata, K., Spectrophotometry of intact biological materials. Absolute and relative

measurements of their transmission, reflection and absorption spectra, *J. Biochem.*, 45, 599–623, 1958.

Smith, R. C., and K. S. Baker, Optical properties of the clearest natural waters (200–800 nm), *Appl. Opt.*, 20, 177–184, 1981.

Smith, R. C., and K. S. Baker, Oceanic chlorophyll concentrations as determined by satellite (Nimbus-7 Coastal Zone Color Scanner), *Mar. Biol.*, 66, 269–279, 1982.

Table 1. Parameters for the Case 2 chlorophyll algorithm for regions without packaged pigments; see text for definitions.

wavelength dependent parameters					
λ	412	443	490	510	555
b_{bw} (m^{-1})	0.003341	0.002406	0.001563	0.001313	0.000929
a_w (m^{-1})	0.00480	0.00742	0.01632	0.03181	0.05910
a_0	2.20	3.59	2.27	1.40	0.42
a_1	0.75	0.80	0.59	0.35	–0.22
a_2	–0.5	–0.5	–0.5	–0.5	–0.5
a_3	0.0112	0.0112	0.0112	0.0112	0.0112

wavelength independent parameters					
X_0	–0.00182	S	0.0225	c_0	0.2818
X_1	2.058	p_0	51. 9	c_1	–2.783
Y_0	–1.13	p_1	1.00	c_2	1.863
Y_1	2.57			c_3	–2.387

Table 2. List of cruises with optical and bio-optical data collected by the University of South Florida (Carder data set). Numbers in parenthesis in the far left column indicate the number of stations included in the global evaluation data set.

cruise	start date	end date	region	# stations
MLML 2	13 Aug 91	29 Aug 91	North Atlantic, 42°N–60°N	7 (3)
TT010	20 Jul 92	02 Aug 92	North Pacific, 24°N–48°N	10 (10)
GOMEX	10 Apr 93	19 Apr 93	Northern Gulf of Mexico	21 (17)
COLOR	31 May 93	09 Jun 93	Northern Gulf of Mexico	13 (4)
TN042	29 Nov 94	18 Dec 94	Arabian Sea	12 (12)
TN048	21 Jun 95	13 Jul 95	Arabian Sea	41 (41)
				total =104(87)

Table 3. Algorithm parameters used with the "packaged" and modified global data sets. All algorithm parameters not listed here are the same as in Table 1. The values of $a_3(\lambda)$ shown apply to all of the SeaWiFS wavelengths. The equation to determine chl *a* from $a_\phi(675)$ for this data set is given by Equation 21.

parameter	packaged	global
$a_0(412)$	1.90	1.95
$a_0(443)$	2.70	2.95
$a_0(490)$	1.90	1.99
$a_2(\lambda)$	-0.45	-0.5
$a_3(\lambda)$	0.021	0.025
p_0	74.1	72.4
p_1	1.0	1.0
p_2	0.0	0.0
c_0	0.4818	0.3147
c_1	−2.783	−2.859
c_2	1.863	2.007
c_3	−2.387	−1.730

Table 4. Summary of regression statistics for each data set tested. The unpackaged data consists of the Carder, EqPac above-surface, EqPac below-surface, Taiwan, and MOCE3 data sets. The packaged data consists of the CalCOFI, and CAL9704 data sets. The global data consists of the global evaluation data set, minus the Cota and U. Maryland data plus the high-chlorophyll Carder, EqPac above-surface, Taiwan, and MOCE3 data, and uses one set of average algorithm parameters for the whole data set. SA indicates that only the modeled values that passed the semi-analytical portion of the algorithm are used (including blended values). SA+EMP indicates that all modeled values—semi-analytical, blended, and empirical—are used. All statistics except RMS2 are calculated from $\log_{10}$-transformed variables.

data set	variable	n	intercept	slope	bias	R^2	RMS1	RMS2
Carder	chl SA	86	0.019	1.020	0.010	0.921	0.122	0.289
Carder	chl SA+EMP	104	–0.007	0.977	–0.002	0.963	0.132	0.300
Carder	$a_\varphi(675)$ SA	82	0.098	1.052	–0.008	0.898	0.131	0.302
Carder	$a_g(400)$ SA	26	–0.278	0.905	–0.186	0.751	0.252	0.405
unpackaged	chl SA	261	0.001	0.999	0.002	0.873	0.099	0.230
unpackaged	chl SA+EMP	278	-0.019	0.973	-0.003	0.955	0.108	0.242
packaged	chl SA	303	-0.006	0.999	-0.006	0.917	0.111	0.268
packaged	chl SA+EMP	326	0.004	1.012	-0.003	0.951	0.114	0.282
global	chl SA	883	0.002	1.003	0.002	0.852	0.176	0.446
global	chl SA+EMP	976	0.003	1.003	0.002	0.913	0.174	0.440